Dimerization of a membrane transporter is driven by differential energetics of lipid solvation of dissociated and associated states

Running title: Differential lipid solvation drives CLC-ec1 dimerization.

Rahul Chadda[1*], Nathan Bernhardt[3*], Elizabeth G. Kelley[4], Susana C. M. Teixeira[4,5], Kacie Griffith, Alejandro Gil-Ley[2,3], Tuğba N. Öztürk[1], Lauren E. Hughes[2], Ana Forsythe[2], Venkatramanan Krishnamani[2], José D. Faraldo-Gómez[3#] and Janice L. Robertson[1#]

[*]equal contribution

[#]corresponding authors

[1]Biochemistry and Molecular Biophysics, Washington University School of Medicine, St. Louis, MO 63110

[2]Molecular Physiology and Biophysics, Carver College of Medicine, The University of Iowa, Iowa City, IA 52242

[3]Theoretical Molecular Biophysics Laboratory, National Heart, Lung and Blood Institute, National Institutes of Health, Bethesda MD 20892

[4]Center for Neutron Research, National Institute for Standards and Technology, Gaithersburg, MD 20899

[5]Center for Neutron Science, Chemical and Biomolecular Engineering, University of Delaware, Newark DE 19716

ABSTRACT

Over two-thirds of membrane proteins of known structure assemble into oligomers. Yet, the forces that drive the association of these proteins in the membrane remain to be delineated, as the lipid bilayer is a solvent environment that is both structurally and chemically complex. In this study we reveal how the lipid solvent defines the dimerization equilibrium of the CLC-ec1 Cl^-/H^+ antiporter. Integrating experimental and computational approaches, we show that monomers associate to avoid an energetic penalty for solvating a thinned-membrane defect caused by their exposed dimerization interfaces. Supporting this theory, we demonstrate that this penalty is drastically reduced with minimal amounts of short-chain lipids, which stabilize the monomeric state by preferentially solvating the defect rather than altering the physical state of the membrane. We thus posit that the energy differentials for local lipid-solvation define membrane-protein association equilibria, and describe a molecular-level physical mechanism for lipid regulation of such processes in biological conditions.

INTRODUCTION

Lipid bilayers are the most common means of chemical compartmentalization in biology. The bilayer interior, formed by the acyl chains, is a ≈ 30 Å layer of low-dielectric fluid oil (Fricke, 1925) that provides a natural electrostatic barrier for the passage of charged and polar species. This insulating core enables the cell to generate trans-bilayer chemical and electrical potential-energy gradients that fuel essential metabolic functions. While the macroscopic structure of the lipid bilayer is shared across nearly all species and organelles, their chemical composition is remarkably diverse. For example, phospholipids can vary in their headgroup moieties, in the length and degree of saturation of the acyl chains, and in the chain-headgroup linkage, i.e. ester vs. ether (Meer et al., 2008). Acyl-chains can feature modifications such as branching, or even form covalent bonds across monolayers, as in tetraether lipids (Valentine, 2007). Lipidomics studies show that cellular membranes can be comprised of hundreds of lipid types (Brügger, 2014), and that composition can change under different physiological conditions (Marr and Ingraham, 1962; Sanders and Mittendorf, 2011). Why is there so much variability, when the basic features of any of these molecules are sufficient to provide a fluid lipid bilayer barrier?

The answer to this question may lie in the fact that ≈ 25% of the total membrane area consists of embedded proteins (Phillips, 2018). The mechanisms of these proteins are, fundamentally, not unlike those of water-soluble proteins and entail processes such as molecular recognition, conformational exchange and catalyzed chemistry. For membrane proteins, however, the lipid bilayer provides a distinct reaction environment where lipid molecules are the primary solvent. As is the case for any biological equilibrium reaction, the solvent plays a major role in defining the energetic landscape. It seems therefore logical to hypothesize that the variability in the chemical composition of physiological membranes reflects an innate ability of the membrane to modulate protein structure and function.

Here, we consider the role of the lipid bilayer in a highly prevalent reaction in membrane biology - protein oligomerization. Indeed, among membrane-protein classes of known structure, ≈ 70% are found as homo- or hetero-oligomers (Aleksandrova et al., 2019). Yet, the physical factors controlling membrane-protein assembly in membranes are largely unknown. Naturally, the first recourse is to consider what we have learned for protein oligomers that reside in water. For these complexes, it has been found that the hydrophobic effect is a principal driving force, i.e. non-polar protein-protein interfaces are driven together to avoid the energetic penalty associated with the diminished entropy of the water molecules solvating those hydrophobic surfaces, relative to bulk water (Tanford, 1978). When examining membrane protein

68 oligomers, it is typical that non-polar surfaces also become buried in the associated complex. However,
69 the membrane contains little water and so the hydrophobic effect cannot be a dominant factor.
70 Alternatively, it has been proposed that in membrane proteins, the burial of non-polar interfaces brings
71 many hydrophobic side-chains into close proximity, conferring stability by increasing protein-protein van
72 der Waals interactions. Yet, the degree to which this drives association remains an open question as these
73 side chains also form extensive contacts with lipids in the dissociated states, and so it is unclear whether
74 there are actually net favorable interactions. By analogy, polar interactions between proteins are not the
75 primary force driving their oligomerization in water. It is thus unclear that a physical intuition about
76 protein oligomerization in the membrane can be directly inferred from our understanding of this process
77 in water, because the solvents in these two reaction environments are so drastically different.

78 Nonetheless, the statistical-molecular perspective so elegantly reflected in the hydrophobic effect
79 theory does suggest that in order to understand oligomerization in membranes, we must consider
80 analogous complexities associated with lipid solvation. Specifically, we must examine what differences
81 exist in the interplay between the lipid solvent and the 'reactants' and 'products' involved in the reaction.
82 Indeed, optimal 'solvation' of dissociated and associated states might entail distinct spatial distributions
83 of the bilayer lipid components, distinct local morphologies, or both. These differences will necessarily
84 translate into an energetic cost, which conceivably might be large enough to control the oligomerization
85 equilibrium. In this perspective, the free energy of association, or any other conformational reaction,
86 depends on the chemical and physical nature of the lipid solvent and how it defines the magnitude of the
87 energy differential between endpoint states. This reasoning leads to the hypothesis that variations in
88 membrane composition in different physiological conditions could regulate oligomerization equilibria by
89 altering the energetics of local lipid solvation effects, even when those variations do not translate into
90 global changes in the physical state or morphology of the membrane.

91 A key to evaluating whether differences in lipid solvation can be a dominant driving force for
92 membrane protein oligomerization is to develop assays to accurately quantify this kind of equilibria in
93 lipid bilayers. Previously, we established such an assay based on single-molecule fluorescence
94 microscopy, and carried out measurements of the free-energy of dimerization of the *E. coli* Cl^-/H^+
95 antiporter complex CLC-ec1 (**Figure 1A**) in 2:1 palmityl, oleoyl phosphatidyl-
96 ethanolamine/phosphatidyl-glycerol (2:1 POPE:POPG) lipid bilayers (Chadda et al., 2016). These
97 membranes are a synthetic mimic of the *E. coli* polar-lipid composition, containing $C_{16:0,18:1}$ tails, the most
98 common acyl chain in biological membranes (Phillips, 2018). While CLC-ec1 forms homodimers in

99 detergent and membranes (Maduke et al., 1999; Dutzler et al., 2002), our measurements revealed this
100 protein complex results from association of two functionally competent monomers (Robertson et al., 2010)
101 via a membrane-embedded hydrophobic interface (**Figure 1B**), with an equilibrium dimerization free
102 energy of -10.9 kcal/mole, relative to a standard state of 1 monomer/lipid (Chadda et al., 2018). This is a
103 remarkable finding, implying that the population of dissociated monomers in biological conditions is
104 virtually zero. As mentioned above, it is hard to rationalize how this strong association could result solely
105 from the conversion of monomer-lipid contacts into monomer-monomer contacts.

106 To address this, we set out to investigate the hypothesis that dimerization of CLC-ec1 is driven by
107 the differences in lipid solvation energies of the dimer and monomer states, which translate into an
108 effective attractive force. First, we use molecular dynamics simulations of monomeric and dimeric CLC-
109 ec1 in 2:1 POPE:POPG to understand the lipid solvation structure in each state. This analysis informs a
110 set of new experimental assays, namely small-angle neutron scattering measurements, Cl^- transport assays
111 and single-molecule photobleaching analyses, with which we quantify how addition of short chain $C_{12:0}$,
112 di-lauryl (DL) lipids alters the dimerization equilibrium in membranes. To obtain a molecular level
113 interpretation of these new experimental results, we return to molecular dynamics simulations in
114 membrane mixtures that mimic the experimental conditions. We find that lipid solvation of the exposed
115 dimerization interfaces results in a strong energetic penalty for the monomeric state. Burial of these
116 interfaces during dimerization relieves this penalty, translating the lipid solvation effect into an attractive
117 force. Accordingly, this stabilizing force is tunable through addition of lipids that minimize the
118 abovementioned energetic penalty by acting as a 'better' solvent for the dimerization interface. From a
119 fundamental perspective, this study suggests a molecular framework for interpreting the role of lipids in
120 membrane-protein self-assembly. From a biological standpoint, our results demonstrate how minimal
121 changes in lipid composition can have a profound effect on membrane protein equilibria, presenting a
122 rationale for why biological membranes possess such diversity in their chemical compositions.

123 **RESULTS**

124

125 **The dimerization interface of CLC-ec1 introduces a structural defect into the surrounding**
126 **membrane.**

127

128 Dimerization of the CLC-ec1 Cl^-/H^+ antiporter buries ≈ 1200 $Å^2$ of non-polar surface in each monomer
129 (**Figure 1A, 1B**). These surfaces exhibit high shape-complementarity, implying many non-polar residues
130 come into close contact (Robertson et al., 2010). Yet, it is not evident that these contacts are the primary
131 cause of dimerization, since it would appear that just as many hydrophobic contacts between these residues
132 and the surrounding lipids are lost upon complex formation. Thus, while protein-protein contacts and
133 interfacial complementarity may play a role, we reasoned that other factors must explain the very strong
134 propensity of this transporter to dimerize. Intriguingly, examination of the dimerization interface (**Figure**
135 **1B**) shows that the two central helices are much shorter than what is typical in transmembrane helices,
136 implying they may create a 'hydrophobic mismatch' between the protein surface and the surrounding
137 membrane when exposed in the monomeric state (**Figure 1C**). Thus, we hypothesized that energetic
138 penalties associated with solvating the monomer could result in an effective driving force towards
139 dimerization; by burying these 'problematic' interfaces away from the lipids upon association, the system
140 would gain free energy irrespective of the balance between protein-lipid contacts lost and protein-protein
141 contacts formed (**Figure 1D**).

142 To begin to validate or refute this hypothesis, we first examined whether lipid solvation of the
143 exposed dimerization interface indeed results in an energetic penalty. To this end, we studied the structure
144 of the lipid bilayer around the CLC-ec1 monomer and dimer, using coarse-grained molecular dynamics
145 (CGMD) simulations. In both cases we used 2:1 POPE/POPG membranes (**Figure 2 - Figure Supplement**
146 **1A**), corresponding to the $C_{16:0,18:1}$ acyl-chains used in our previous experimental measurements of the
147 reversible dimerization reaction (Chadda et al., 2016). Any simulation of a non-homogenous membrane
148 necessarily presupposes an initial spatial distribution of the lipid components, which is not only arbitrary
149 but also may not be representative of the equilibrium condition. Prior to examining the structure of these
150 membranes, it is therefore key to ascertain that the simulations are long enough for the two lipid
151 components to mix fully and spatially re-distribute according to the energy landscape of the molecular
152 system. One way to examine this process of mixing is to quantify, for each lipid in the simulation box,
153 what fraction of all other lipids in the same leaflet are at some point part of their first solvation shell. In

154 our case, this analysis shows that each lipid, on average, is in direct contact with 80% of all other lipids in
155 the course of each of our simulations (i.e. over 1,100 molecules) (**Figure 2 - Figure Supplement 1B**).
156 Given that at any given timepoint, a solvation shell consists of fewer than 10 lipids, this result implies
157 extensive mixing and hence no concerns in regard to the starting condition. We also examined the
158 orientation of the protein in the bilayer, which is also an arbitrary initial condition. This analysis indicates
159 that the simulations broadly explore orientation space, resulting in clearly defined probability distributions
160 for both monomer and dimer (**Figure 2 - Figure Supplement 1C)**.

161 With sufficient lipid exchange over the time-scale of the simulations, we analyzed the shape of the
162 lipid bilayer near the monomer and the dimer as well as other structural descriptors (Figure 2 - Figure
163 Supplement 2). From the simulated trajectories, we calculated 3D density maps reflecting the spatial
164 distribution of both acyl-chains and ester linkages in the protein vicinity (**Figure 2A, B**). The results for
165 the monomer show that the membrane shape is deformed at the dimerization interface, thinning near the
166 two shorter helices at the center. Elsewhere along the monomer perimeter the membrane is largely
167 unperturbed, and its shape is nearly identical to what we observe for the dimer, confirming the simulations
168 are probing the membrane structure reliably. Quantitative analysis of bilayer thickness, measured by the
169 separation between the outer and inner ester layers and represented on a 2D color map, shows that the
170 magnitude of this thinning defect is ≈ 8 Å relative to the bulk (**Figure 2C**), i.e. nearly a quarter of the
171 unperturbed hydrophobic membrane thickness. This defect is also clearly specific to the dimerization
172 interface in the monomeric state; consistent with the 3D density maps. Smaller defects are discernable
173 elsewhere, but are indistinguishable between monomer and dimer.

174 Continuum models of hydrophobic mismatch conceptualize membrane thickness deformations as
175 resulting from spring-like compressions or extensions of the lipid chains (Andersen and II, 2007; Brown,
176 2017). However, our calculations show that the mean alkyl-chain end-to-end distance is reduced only by
177 a fraction of 1 Å relative to the bulk value for positions near the protein (**Figure 2 - Figure Supplement**
178 **3A**); this minor perturbation is also not specific to the dimerization interface, but is present at other
179 regions. Therefore, the thinning defect that we observe does not result from compression of the alkyl-
180 chains. By contrast, analysis of the orientation of the acyl-chains, in terms of the coarse-grained equivalent
181 of a second-rank order parameter, reveals a clear change at the dimerization interface (**Figure 2 – Figure**
182 **Supplement 3B**). To evaluate this effect in more detail, we examined how the mean lipid-chain tilt angle
183 varies across the system, relative to the membrane normal (**Figure 2D**). In the bulk, this angle averages
184 to 0° for one leaflet and 180° for the other, as the lipid dynamics are isotropic on the membrane plane. At

185 the dimerization interface, however, there is a focused region in which this angle is deflected by 60° in
186 both leaflets. This drastic change in orientation can be visualized by analyzing the "average structure" of
187 lipid molecules in different positions across the membrane (**Figure 2E**). In the bulk this average is a linear
188 structure, perfectly perpendicular to the membrane mid-plane, again due to the isotropy of the lipid
189 configurational dynamics. However, the lipids that are closest to the dimerization interface (green helices)
190 adopt tilted, non-bilayer configurations in order to optimally solvate the protein. Alongside this change
191 in tilt angle we observe that the alkyl-chains near the dimerization interface have increased contacts with
192 lipids in the opposing leaflet (**Figure 2F**) and show a greater degree of inter-digitation (**Figure 2 – Figure**
193 **Supplement 3C**), compared to the bulk or elsewhere along the protein perimeter. Another revealing
194 metric is the lipid density, quantified here as the number of lipid neighbors within a certain distance
195 threshold (**Figure 2G**). Naturally, this metric gradually diminishes near any of the protein interfaces;
196 however, the data reveals a much more pronounced and long-ranged density defect at the dimerization
197 interface, particularly at the level of the ester and headgroup layers. Indeed, this lipid packing defect is
198 such that the degree of water penetration of the membrane interior approximately doubles, relative to the
199 bulk value (**Figure 2H**).

200 In summary, our simulation data clearly shows that when the dimerization interface of CLC-ec1
201 is exposed to the lipid solvent, it deforms the surrounding membrane by thinning and twisting the bilayer
202 structure. To solvate this 'problematic' interface, $C_{16:0,18:1}$ lipids must adopt non-bilayer configurations
203 that are significantly tilted and more loosely packed and thus more permissive to water penetration.
204 Interestingly, the perturbations we observe are in all cases symmetric with respect to the bilayer midplane,
205 consistent with the fact that the CLC-ec1 monomer consists of two topologically inverted structural
206 repeats. All of these observations, along with the fact that the solvation structure deviates drastically from
207 the intrinsic propensities of the bulk bilayer, indicate that optimal lipid solvation of the monomeric state
208 requires the membrane to adopt a high energy conformation. Even if lipid solvation of the dimer may
209 entail an energetic penalty, the cost will be less than that of solvating two dissociated monomers.

210 To substantiate this notion quantitatively, we also simulated a pure 2:1 POPE-POPG bilayer (i.e.
211 with no protein) and based on analysis of the spontaneous, molecular-scale fluctuations in bilayer
212 thickness, we calculated the 1D potential of mean force (PMF) free-energy curve that governs these
213 dynamics (**Figure 2I**). Using this data, we translated the 2D maps of local membrane thickness obtained
214 from simulations in the presence of CLC-ec1 (**Figure 2C**) into 2D maps of the corresponding free-energy
215 cost (**Figure 2I**). Integrating these data over the first solvation shell (≈ 10 Å from the protein surface)

216 confirms that for $C_{16:0,18:1}$ lipids, solvation of the thinning defect caused by the exposed dimerization
217 interface is costly, namely ≈ 10 kcal/mole per monomer. That is, from the standpoint of lipid-solvation
218 energetics, as it pertains to bilayer thickness, dimerization results in free-energy gain of ≈ 20 kcal/mole.
219 While other contributions surely exist, both favorable and unfavorable, it is clear that the energy penalty
220 resulting from lipid solvation of the monomer is a dominant factor in driving the association of CLC-ec1
221 dimers.
222
223 **Reducing the cost of lipid solvation of the dimerization interface with short-chain lipids.**
224
225 If solvation of the membrane defect caused by monomeric CLC-ec1 in $C_{16:0,18:1}$ lipids confers an energetic
226 penalty that dominates the dimerization equilibrium, then we hypothesize that this equilibrium should be
227 shifted towards the monomeric state by introducing lipids that are more structurally suited to that
228 perturbation. Since the defect is constructed by hydrophobic thinning, we decided to test this hypothesis
229 by introducing short-chain di-lauryl (DL) $C_{12:0}$ lipids into the $C_{16:0,18:1}$ PO lipid membranes while keeping
230 the overall 2:1 PE:PG headgroup composition constant (**Figure 3A**).
231 DL lipids are shorter than PO lipids by 4-6 carbons per chain, and are also fully saturated, losing
232 the ω-9 double bond in one chain. Before drawing any conclusions in regard to the CLC-ec1 dimerization,
233 we sought to characterize the intrinsic properties of these quaternary lipid bilayers. To do so, we first
234 measured phase-transition thermograms for different DL/PO ratios by differential scanning calorimetry
235 (**Figure 3B**). The mixtures show broad profiles; however, the membranes are fluid at room temperature,
236 with the exception of the 100% DL condition. Plotting the peak T_m as a function of DL shows eutectic
237 behavior with a minimum T_m at ≈ 30% DL (**Figure 3C**). Next, we examined mixed DL/PO liposomes
238 using cryo-electron microscopy imaging. 20% DL membranes were prepared, freeze-thawed into the
239 large multi-lamellar vesicles and then extruded through 400 nm filters. The liposomes and membranes
240 appear similar to those in the 0% DL condition (i.e. 2:1 POPE:POPG), with comparable radius and surface
241 area distributions (**Figure 3D-F**). There is however a small shift of the distributions towards larger
242 liposomes, with 44% of liposomes being multi-lamellar for 20% DL, compared to 25% for PO. Next, we
243 examined the structure of the DL/PO bilayers at 25 ℃ with small-angle neutron scattering (SANS). Using
244 a spherical, multi-lamellar liposome model to fit the scattering spectra (**Figure 3G,H**), we observe a
245 gradual decrease in the bilayer thickness as the DL content is increased (**Figure 3I**); at 90-100% DL, the
246 membrane is ≈ 6 Å thinner than that with no DL. This change is consistent with the published SANS

247 measurements of POPC vs. DLPC (Kučerka et al., 2011) and POPG vs. DLPG (Pan et al., 2014). It also
248 matches the magnitude of the defect created by the CLC-ec1 monomer (**Figure 2C**), indicating that the
249 DL lipids in these mixtures might be suitable for solvating the dimerization interface. Thus, to better
250 understand the nature of this thinning effect, we carried out and analyzed a series of MD simulations of
251 DL/PO lipid bilayers analogous to those evaluated experimentally. Notwithstanding the approximations
252 inherent to the CG forcefield, the simulations reproduce the observed membrane thinning induced by DL
253 lipids (**Figure 3I, Figure 3 – Figure Supplement 1A**). Further analysis of the simulation data also reveals
254 that the variation in membrane thickness upon DL addition appears to be the result of a driving force
255 whose effect is to maintain the overall number of contacts formed between the alkyl-chains in one leaflet
256 and those in the other, regardless of the DL/PO content (**Figure 3 – Figure Supplement 1B**).

257 Having confirmed that DL/PO mixtures form fluid lipid bilayers with an appropriate decrease in
258 membrane thickness, we next examined whether the CLC-ec1 protein remained functional in the new
259 membrane environment. To study this, we carried out chloride efflux measurements from CLC-ec1
260 proteo-liposomes (Walden et al., 2007) to quantify the transport activity as a function of DL in the
261 membrane. The protein was effective at transporting chloride when DL was present (**Figure 4A**), and we
262 observed no difference in the fraction of inactive vesicles, $F_{0,\mathrm{vol.}}$ (**Figure 4B**), or chloride efflux rate, k_{p}
263 (**Figure 4C**) for samples with less than 20% DL. However, at higher DL proportions, we observed that
264 the rate of chloride efflux becomes slower, indicating a loss of activity as DL increases. By comparing
265 the normalized change in activity, Δk_p, and fraction of active vesicles, $\Delta(1-F_{0,\mathrm{vol}})$, with the change in
266 bilayer thickness from the SANS data, Δd_{B}, we find that there is a correlation of the loss of transport
267 activity with the overall thinning of the membrane (**Figure 4D**).

268 Having ascertained that there is no change in CLC-ec1 structure/function in mixed DL/PO
269 membranes where DL $<$ 20%, we investigated the monomer-dimer equilibrium at these conditions, using
270 the single-molecule photobleaching subunit-capture method we previously established (Chadda et al.,
271 2016; Chadda and Robertson, 2016). In this approach, the protein is site-specifically labelled with a Cy5-
272 maleimide fluorophore and reconstituted into lipid bilayers that are fused into large multilamellar vesicles
273 by freeze/thaw cycles. In this state, the membrane area is sufficiently large and the protein density
274 sufficiently low to permit monomer and dimer populations to equilibrate according to the association
275 constant of the reaction, which depends on the protein to lipid mole fraction, χ_{protein}. The oligomeric-state
276 distribution resulting from this equilibrium condition is quantified by fragmenting the membranes into
277 fixed liposome compartments via extrusion, and by counting the probability distribution of subunit capture

278 in the known liposome size distribution. Occupancies are measured using single-molecule photobleaching
279 analysis via total internal reflection fluorescence microscopy, and the photobleaching probability
280 distribution follows a Poisson distribution if one considers heterogenous compartments and multiple
281 protein species (Cliff et al., 2019). Example images and raw data for the photobleaching traces for PO
282 and 20% DL liposomes (**Figure 5A,B)** demonstrates no changes in the quality of images obtained in the
283 different lipid conditions.

284 The photobleaching probability distributions obtained in the subunit-capture method contain
285 information about the dimerization equilibrium, but they also depend on the protein labeling yield and
286 liposome size distribution. Our site-specific labeling procedure allows us to achieve a consistent labeling
287 yield; thus, as long as the we know the liposome size distribution, we can determine the fraction of dimers
288 within our population as a function of the protein density. It is conceivable that changes in the lipid
289 composition could alter the extruded liposome size distribution or introduce other biases into the subunit-
290 capture approach, and so we evaluated these potential effects in two ways. First, as described previously,
291 we directly measured the size distribution by cryo-electron microscopy (**Figure 3D-F**). We observed that
292 the size distribution for 20% DL liposomes is comparable to the 2:1 POPE:POPG liposomes, with a slight
293 shift towards larger liposomes. Second, we also examined the photobleaching probability distributions of
294 two experimental controls: I201W/I422W, referred to as 'WW', a version of the protein with two
295 tryptophan substitutions at the dimerization interface (Robertson et al., 2010) that reports the fixed
296 monomer probability distribution; and R230C/L249C, or 'RCLC', a disulfide cross-linked constitutive
297 dimer (Nguitragool and Miller, 2007) that reports the fixed dimer probability distribution (Chadda et al.,
298 2018). Photobleaching analysis of these controls in 20% DL liposomes show dependencies on the protein
299 mole fraction comparable to those observed for the 2:1 POPE:POPG composition (**Figure 5 – Figure**
300 **Supplement 1A,B**). However, we also observe a small increase in the saturation of liposomes, as
301 indicated by the steeper decay in single-step photobleaching probabilities, P_1, and increased rise in the P_{3+}
302 probabilities, at higher protein densities. This behavior could arise from an increase in larger liposomes
303 within the population, in agreement with our findings from the cryo-EM distributions. Altogether, we can
304 conclude that there are no major differences in the liposome size distributions that precludes our
305 interpretation of the photobleaching data; yet, these results also show how photobleaching analysis can
306 provide benchmark data on the underlying liposome population.

307 With our quantification method benchmarked, we then analyzed the monomer-dimer reaction for
308 WT CLC-ec1 in 2:1 PE:PG 20% DL lipid bilayers (**Figure 5C**). Calculation of the fraction of dimer in
309 these protein populations, from least-squares fitting to the WW and RCLC reference distributions, shows
310 that the dimer is significantly destabilized, i.e. the equilibrium is shifted towards the monomeric
311 state (**Figure 5D**). By fitting to an equilibrium dimerization isotherm, we estimate a lower-limit of the
312 $K_D > 4.2 \times 10^{-6}$ subunit/lipid, as the reaction falls out of the dynamic range for these measurements leading
313 to an insufficient fit of the reaction, but indicates that the 20% DL condition destabilizes dimerization by
314 at least +3 kcal/mole. As a final test, we examined whether the mostly dimeric population of CLC-ec1 in
315 2:1 POPE:POPG lipid bilayers is driven towards the monomer state when fusing these proteo-liposomes
316 with DL containing membranes. **Figure 5E** shows the resultant distribution of diluting $\chi_{protein} = 2 \times$
317 10^{-6} subunits/lipid proteoliposomes 1:1 via freeze-thawed fusions with either 0% DL or 40% DL (i.e. final
318 DL proportion is 20%). Indeed, after incubating the fused samples for 5 days at room temperature (**Figure**
319 **5 – Figure Supplement 1C,D**), the probability distribution showed a significant shift towards monomers,
320 indicated by an increase in single steps, P_1. Therefore, alternative approaches consistently demonstrate
321 that the short-chain DL lipid shifts the oligomeric distribution of CLC-ec1 towards monomers.
322 To examine how dimerization depends on the DL/PO ratio, we carried out a titration experiment,
323 studying the monomer-dimer distribution as a function of DL %, from 10^{-8} to 80% DL (**Figure 5F**). Note
324 these experiments are conducted at dilute protein densities within the membrane, with 1 subunit per
325 million lipids ($\chi_{protein} = 1 \times 10^{-6}$ subunits/lipid), where WT CLC-ec1 is ≈ 80% dimeric in 2:1
326 POPE/POPG. The raw photobleaching probability distribution shows a population shift from nearly all
327 dimers in 0% DL ($P_1 \approx P_2$) to all monomers at 80% DL ($P_1 > P_2$), which resembles the distribution of
328 WW in 2:1 POPE/POPG. Calculation of F_{dimer} from these data shows that the impact of DL on
329 dimerization follows two phases, namely a gradual, non-saturating decrease up until 1% DL (**Figure 5G**),
330 then a steep conversion to all monomers for DL > 1%. This observation indicates CLC-ec1 dimerization
331 is modulated by the presence of DL via two distinct processes, that occur when there are no changes in
332 bulk bilayer thickness. This is a key finding, which becomes apparent if the normalized change in the
333 dimeric population, ΔF_{dimer}, and the change in the bilayer thickness from the SANS data, Δd_B, are plotted
334 together for comparison (**Figure 5H**). We observe that both phases of the shift in the dimerization
335 equilibrium occur well below 20% DL, i.e. before there are any major changes in the macroscopic
336 structure of the membrane or the protein. This result clearly demonstrates that this equilibrium is not
337 directly coupled to the macroscopic bilayer thickness, unlike the transport activity, but it is instead

338 dependent on a microscopic process effected by DL, detectable even when DL is present in minimal
339 amounts. Converting F_{Dimer} to the change in free energy of dimerization relative to the zero DL condition,
340 ΔΔG, shows that there is a shift of ≈ +1.5 kcal/mole between 0-1 % DL, followed by a +0.87 ± 0.27
341 kcal/mole destabilization per additional 10% increment in DL beyond 1% DL (**Figure 5I**).
342
343 **Enrichment of DL at the CLC-ec1 dimerization interface.**
344
345 To investigate the mechanisms by which addition of DL shifts CLC-ec1 dimerization equilibrium toward
346 monomers, we again turned to CGMD simulations. Specifically, we carried out simulations of the
347 monomer in bilayers of DLPE/DLPG/POPE/POPG lipids with a 2:1 PE:PG ratio and a DL content of
348 either 1%, 10%, 30% or 50% (**Figure 6 - Figure Supplement 1A**). Before drawing any conclusions from
349 these simulations, we ascertained that this complex bilayer does appropriately mix in the timescale of the
350 trajectories, using a metric identical to that considered for the POPE/POPG simulations. Taking the 50%
351 DL membrane as an example, we observe that by the end of the simulations, any one PO or DL lipid has
352 been in direct contact with ≈ 90% of all other lipid molecules in the same leaflet (**Figure 6 - Figure**
353 **Supplement 1B**), indicating near-ideal equilibration. We then proceeded to examine the structure of these
354 membranes using the same descriptors as those employed above. Interestingly, the thinned defect around
355 the dimerization interface, is still observed in the mixed DL/PO simulations, even for 50% DL (**Figure**
356 **6A, B**), and is comparable to what we find in the 2:1 POPE:POPG simulations (**Figure 2C,D**). That is,
357 the defect is observed even when the 'macroscopic' thickness of the lipid bilayer is reduced (**Figure 3I**).
358 Examination of 3D density maps for the first lipid solvation shell demonstrates that both PO and DL lipids
359 solvate the totality of the protein surface, though not identically (**Figure 6C**). At the two interfaces not
360 involved in dimerization, the DL density signal weakens at the center of the membrane, revealing the DL
361 chains are too short to solvate the hydrophobic span of the protein, which is better matched to PO.
362 Conversely, the density signal for PO is weaker than DL at the dimerization interface, and weaker than
363 that seen in the 100% PO membrane, indicating PO is depleted here. This depletion, and the corresponding
364 enrichment in DL lipids, becomes apparent in 2D projections of the percent difference between the
365 observed lipid density ratio (DL/PO) and the expected bulk ratio (**Figure 6D**). These data show that the
366 normalized probability of observing DL rather than PO at the dimerization interface is higher than
367 elsewhere in the membrane, irrespective of PO/DL composition. Conversely, DL is depleted at the other
368 two interfaces, consistent with the 3D density analysis discussed above. Quantification of the DL

369 enrichment as a function of the distance from the protein surface reveals this effect extends for up to 30
370 Å from the dimerization interface, and confirms that it is largely independent of the PO/DL ratio (**Figure**
371 **6E**).

372 The observation of near complete lipid mixing in our simulations implies that the enrichment of
373 DL at the dimerization interface is neither artifactual nor transient but rather a minimum free-energy state
374 of the lipid-solvent structure. What are the molecular factors that explain this observation, i.e. what drives
375 the preferential residence of DL over PO in this specific region of the membrane? As discussed above,
376 analysis of pure PO/DL bilayers shows that while the bilayer thickness decreases with increasing DL
377 content, the number of hydrophobic contacts between the two leaflets is, on average, constant (**Figure 3**
378 **– Figure Supplement 1B**). This observation might seem surprising, given that DL lipids are shorter than
379 PO. Indeed, we observe that DL lipids do not contribute nearly as many contacts as PO, even in the 50%
380 DL condition. However, this diminishing effect is fully compensated by PO lipids, which become more
381 interdigitated as DL content increases so as to preserve the total number of contacts irrespective of the
382 PO/DL ratio.

383 With this observation in mind, examining the average configurations of the PO and DL lipids in
384 the CLC-ec1 system (**Figure 6F**) reveals key differences that explain why DL is enriched at the
385 dimerization interface. In the bulk, both lipids are configured like in the pure-lipid simulation, i.e. PO
386 lipids exhibit a greater degree of interdigitation and number of contacts in the opposing leaflet than DL
387 lipids (**Figure 6F**), and also greater than PO in the absence of DL (**Figure 2E**); as a result, the total number
388 of interleaflet contacts is a conserved quantity across conditions (**Figure 3 - Figure Supplement 1B**). At
389 the CLC-ec1 dimerization interface, however, this conserved quantity can only be matched by DL lipids,
390 while the presence of PO lipids results in an excessive, clearly atypical overlap between leaflets (**Figure**
391 **6F,G**). The enrichment in DL also diminishes the lipid packing defect observed in PO (**Figure 6H**), which
392 leads to a clear reduction in water penetration of the bilayer interior (**Figure 6I**,**J**). Thus, while key
393 features of the membrane perturbation caused by the CLC-ec1 monomer are not fundamentally altered by
394 addition of DL, solvation of this defect with DL lipids does imply that the bilayer can conserve its inherent
395 bulk-like characteristics to a greater extent, while the opposite is true for PO. Therefore, we can infer that
396 in the PO/DL conditions the energetic cost of lipid solvation of the monomer is reduced, relative to the
397 pure PO condition. This preferential solvation effect would in turn explain the shift in dimerization
398 equilibrium observed experimentally, particularly at low DL concentrations.

As noted above, increasing DL content results in a change in the overall thickness of the PO/DL bilayers. Thus, it could be reasonably argued that this 'macroscopic' effect, conventionally referred to as "hydrophobic matching", would also reduce the energetic cost of the thinned membrane defect caused by CLC-ec1, irrespective of whether one lipid type or another is preferentially enriched there, and thereby cause a shift the dimerization equilibrium. It is important to note, however, that the enrichment effect we report is discernable at 1% DL, i.e. in conditions where there is virtually no change in the global thickness of the bilayer, relative to the PO condition, both in experiment and simulation (**Figure 3I**). Nevertheless, 1% DL has a profound impact on the dimerization equilibrium. These results underscore that a process distinct from hydrophobic matching is dominant in this regime, which we posit is that of preferential lipid solvation.

DISCUSSION

This study demonstrates that the dimerization of a membrane protein can be driven in large part by the energetic cost of lipid solvation of the monomeric state, due to the exposure of a protein surface that alters the membrane structure. While other factors such as protein-protein interactions may also contribute to the overall stability of the dimer, the significant dependency on membrane forces observed in this study means that this oligomerization equilibrium is a contextual property, i.e. one that depends directly on the chemical and physical nature of the lipid bilayer. In our studies, we observe two mechanisms by which the monomer-dimer free-energy balance can be modulated by lipids: first, preferential solvation, i.e. the recruitment of specific lipid types that are more naturally able to reside in the defect caused by the protein; and second, hydrophobic matching, whereby the thickness of the bulk membrane approximates that of the defect. While both mechanisms reduce the free-energy cost of solvating the monomeric state, we find that preferential solvation is the dominant effect in a wide range of conditions that also preserve the structure and functionality of the protein; when hydrophobic matching becomes significant, the dimerization equilibrium has been already shifted drastically, and the global changes in the physical state of the membrane degrade the protein functionality. In the following sections, we discuss the molecular intricacies and physiological implications of such findings.

430 **Burial of membrane defects is a significant driving force for CLC-ec1 dimerization.**
431
432 Our computational studies demonstrate that the CLC-ec1 monomer in 2:1 POPE:POPG introduces a non-
433 bilayer thinned defect in the surrounding membrane, due to the exposure of the shorter central helices that
434 form the core of the dimerization interface. This defect translates into an energetic penalty of up to 10
435 kcal/mole per monomer, coming from the lipid bilayer alone; burial of this surface in the dimer therefore
436 offers a stabilization of up to 20 kcal/mole. Experimentally, we have measured that the free energy of
437 CLC-ec1 dimerization in 2:1 POPE/POPG lipid bilayers is -11 kcal/mole (1 subunit/lipid standard state).
438 Thus, it is plausible that dimerization is driven primarily by membrane dependent forces, with protein-
439 protein interactions contributing marginally. Conclusive evaluation of this hypothesis will require further
440 experimental investigations of the dimerization equilibrium for a range of protein constructs in different
441 lipid bilayers and conditions. However, the quantitative analysis presented here already indicates that
442 optimal lipid solvation of the associated and dissociated states entails very different energetic costs, and
443 that this differential would be sufficient to drive oligomerization in membranes.
444 The concept that protein-induced membrane defects can translate into an effective driving force
445 towards oligomerization presents a generalizable solution to the problem of membrane protein self-
446 organization, while allowing for evolutionary adaptations in amino-acid sequence that might be
447 advantageous. In this perspective, association primarily depends on the overall protein architecture and
448 the general chemical features of the protein interfaces. The specific amino-acid composition of the protein
449 surface is thus not critical though not entirely inconsequential. Membrane protein complexes may evolve
450 high shape-complementarity, for example to maximize the exclusion of lipids in the complexed form of
451 the protein (Li et al., 2013), and thereby achieve greater stability. Indeed, previous analysis showed that
452 CLC-ec1 exhibits high shape-complementarity, comparable to other high-affinity antigen antibody
453 complexes (Robertson et al., 2010). A mechanism based on differentials in lipid-bilayer morphology and
454 energetics would also imply that protein homologues in the same family, i.e. sharing the same fold and
455 lipid-interface architecture, would be inherently driven to oligomerize, irrespective of whether the amino
456 acid sequence of the binding interfaces is conserved in a conventional sense.
457 Membrane perturbations appear to influence the association of other membrane protein systems as
458 well. Assembly of Gramicidin peptides into functional ion-channel dimers results in a hydrophobic
459 mismatch with the surrounding bilayer, and thus the dimerization equilibrium can be modulated by
460 adjusting the membrane thickness (Goodall, 1971; Mobashery et al., 1997). Computational studies have

461 proposed that the burial of anisotropic defects is involved in driving oligomerization of G-protein coupled
462 receptors (GPCRs) (Botelho et al., 2006; Mondal et al., 2014, 2011). Indeed, experiments of rhodopsin
463 have revealed that reconstituting the protein in lipids with different chain lengths leads to increased FRET
464 signals corresponding to higher-order macromolecular assemblies (Mondal et al., 2014). Other modeling
465 studies have proposed that burial of anisotropic defects could lead to higher-order aggregation of proteins
466 into membrane meshes (Kahraman and Haselwandter, 2019). A striking illustration of this concept is
467 found in the inner mitochondrial membranes, where ATP synthases, each a dimeric complex,
468 spontaneously align into micron-scale rows, priming the membrane to invaginate and form cristae; this
469 self-organization process occurs without direct protein contacts and is instead driven by the minimization
470 of long-range membrane curvature defects created by the individual complexes (Anselmi et al., 2018).
471 Thus, there is a growing body of evidence that suggests that membrane dependent forces are a key factor
472 in the self-assembly and organization of membrane proteins and their complexes in biological membranes.
473
474 **Preferential solvation vs. hydrophobic matching vs. site-specific binding.**
475
476 The notion that different states of a membrane protein oligomer perturb the bilayer in distinct ways, both
477 structurally and energetically, implies a mechanism through which variations in lipid composition can
478 regulate this type of equilibria. However, alternative mechanisms can be envisaged. If the perturbation
479 created by a protein state is a change in thickness, then the energetics of each state depends on the
480 macroscopic membrane thickness - an effect that has is called 'hydrophobic matching'. Alternatively, a
481 different mechanism could involve the binding of lipids to membrane proteins in a manner similar to
482 conventional agonists or antagonists, thereby influencing their structures or dynamics. While our
483 experimental assays of CLC-ec1 clearly demonstrate that dimerization is dependent on the short-chain DL
484 lipid composition, we discuss in the following sections how neither of these mechanisms are capable of
485 explaining our titration data.
486 The first effect that we observe is when short-chain saturated DL lipids are added to PO bilayers
487 at extremely low DL activities, ranging from 1 DL per 10^{10} PO up to 1% DL. In this regime, we determined
488 that the bilayer thickness is identical to that of PO membranes, and we measure no change in protein
489 function. Yet, upon increasing the amount of DL, we detect a gradual correlated increase in the monomeric
490 proportion of CLC-ec1, and this effect appears to be linear over six orders of magnitude in the % DL
491 (**Figure 5F-H)**. At first, it is intuitive to interpret this data as a process of competitive inhibition, i.e. a

492 DL-specific binding site might exist at the dimerization interface, with an affinity of $K_{D,DL}$, the occupancy
493 of which precludes dimerization. However, we can immediately see that our data do not agree with this
494 type of linkage. This type of model would lead to complete saturation of the population of the monomeric
495 state, over a narrower thousand-fold increase in % DL and centered at the hypothetical $K_{D,DL}$. The gradual,
496 linear decay of the dimeric population that we observe in our data is simply not in agreement with a model
497 of site-specific competitive binding. A hydrophobic matching mechanism can also be ruled out in this
498 regime, given the strong population shift observed without a corresponding change in membrane
499 thickness.

500 Lipid-composition effects can be however conceptualized beyond the paradigms of bimolecular
501 recognition or membrane continuum mechanics. If we consider lipids as solvent molecules, a different
502 type of linkage model, used to examine mixed aqueous solvent systems, explains our observations. The
503 stability of soluble proteins, both as oligomeric assemblies or folds, is known to be dependent on the
504 relative activities of the co-solvents present, due to preferential solvation effects (Tanford, 1969; Record
505 and Anderson, 1995; Schellman, 1987, 2003; Timasheff, 2002; Lee and Timasheff, 1981). That is, one
506 state of the protein might be preferentially solvated by a given co-solvent, and so an increase in that co-
507 solvent activity shifts the reaction equilibrium to that state. This is a form of linkage that describes how
508 proteins can be stabilized or destabilized by salts, glycerol, sugar or chaotropic denaturants. It does not
509 involve specific binding, but rather non-specific affinities that lead to a linear dependency of the change
510 in free energy with the log-activity of the co-solvent, as we observe in our experiments. While this effect
511 had not been previously observed for membrane proteins, it had been discussed as a potential contributing
512 factor to their conformational stability (Marsh, 1995); more recently, CGMD simulations of highly
513 complex bilayers have led to the hypothesis that membrane proteins have unique lipid solvation structures,
514 akin to a "lipid fingerprint" (Corradi et al., 2018). The experiments described here indeed confirm that
515 preferential solvation effects can control membrane protein reactions, and our simulations reveal its
516 molecular basis. Specifically, we observe how at the membrane thinned defect for monomers, the
517 distribution of PO and DL lipids diverges from what would be expected based on their bulk ratio, and the
518 shorter DL lipids become enriched. This enrichment is specific to the dimerization interface, but it is also
519 long-ranged, as opposed to defined only at a particular interaction site. And importantly, it is observed
520 irrespective of the PO/DL content of the bilayer, as could be expected for an effect that is dictated by the
521 protein itself. Although the system must do work to recruit DL molecules from the bulk, this enrichment

522 results in a gain in free energy favoring the monomeric state, as DL is a 'better' solvent for the exposed
523 dimerization interface.
524 As is logical, the preferential solvation effect is ultimately superseded by more global changes in
525 the state of the membrane, which take place when the DL proportion is higher than 10%, according to our
526 SANS experiments. In this regime, we observe an additional depletion of the dimer population, because
527 the energetic penalty of solvating the monomer is further reduced as the membrane becomes thinner. This
528 effect can be thought of as conventional 'hydrophobic matching', specifically for an anisotropic thickness
529 defect created by the protein. However, there are other aspects of the system that are affected in this high-
530 DL range. In particular, we observe a correlated decrease in CLC-ec1 transport activity. That is, while the
531 thinner DL/PO membranes match the exposed dimerization interface better, they also compromise the
532 structural integrity of the protein as a whole. Preferential solvation would thus appear to be a more
533 effective mechanism of lipid regulation of oligomerization reactions.
534
535 **Physiological implications for lipid modulation of membrane proteins.**
536
537 Preferential solvation is a generalizable effect that could modulate any equilibrium whereby one or more
538 protein states introduce a local morphological defect into the membrane. Besides oligomerization
539 reactions, this effect likely defines the energetics of the intermediate conformational states that are
540 encountered during membrane protein folding, as well as gating, transport, and signaling. Given the
541 highly complex composition of actual biological membranes, one can therefore envisage that each of these
542 conformational states will have a different local lipid composition, optimized to stabilize the structure of
543 the membrane in that state. The relative free-energies of the combined protein-membrane system in each
544 state will therefore be dependent on the lipid types that are available, which the cell can alter through e.g.
545 regulation of lipid synthesis and degradation pathways.
546 While membrane protein reactions can be severely influenced in laboratory conditions through
547 drastic changes in the chemical and physical state of membrane, a critical point to note is that a plausible
548 regulatory mechanism must be effective in the actual range that is physiologically viable. Cell membranes
549 are known to undergo changes in lipid composition due to many external factors (Marr and Ingraham,
550 1962; Sanders and Mittendorf, 2011); yet, it is rare for a membrane to change its composition so much
551 that its macroscopic structure is significantly changed. For instance, *E. coli* that is grown at colder
552 temperatures will primarily decrease chain saturation, with only minor changes to the amount of short-

553 chain lipids. The resulting changes are presumed to maintain fluidity while maintaining an appropriate
554 thickness of the membrane so that the majority of membrane proteins remain properly solvated and are
555 still capable of function. As far as we know, there is no situation where a cell will change the overall
556 macroscopic thickness of its membranes due to a physiological stimulus. Therefore, when contemplating
557 possible mechanisms of physiological regulation within the membrane, and particularly with chain-length
558 in mind, we must consider that they should be consistent with low-level changes of these types of lipids
559 within the membrane. Our experiments show that CLC-ec1 dimerization is sensitive to the amount of the
560 short-chain DL lipid in the membrane; even at low levels, from 10^{-8} to 1%, we observe a gradual and non-
561 saturating impact, indicating that dimerization is tunable without a global change in the state of the
562 membrane. The resulting change in the dimer population, from 80% to 50%, could certainly impart a
563 physiological effect if it was linked to a cell signaling function. It is also important to note that the
564 phenomenon of preferential solvation naturally allows for this gradual tuning, as opposed to what would
565 be expected for a process of site-specific lipid-ligand binding, which would inhibit dimerization in a
566 switch-like manner over a much narrower range of DL-lipid concentrations. While site-specific binding
567 mechanisms may be at play for some types of membrane protein processes and specific lipid types, we
568 anticipate that preferential solvation effects will be found to control diverse kinds of membrane protein
569 equilibria in physiological settings.

570 Our examination of the impact of short-chain lipids on CLC-ec1 dimerization sheds light on a
571 potentially ubiquitous mechanism of action by regulatory molecules within the membrane. In simulations,
572 we observe the CLC-ec1 monomers force PO lipids to adopt unnatural configurations, and many of the
573 features of the bilayer near the dimerization interface, ranging from lipid tilt-angle to interleaflet contacts
574 or water exclusion, are radically different from those in the bulk. When DL lipids are present, they
575 spontaneously accumulate at this defect, while maintaining non-specific interactions. In doing so, DL
576 lipids restore some of the bulk-like features to the bilayer near the dimerization interface; thus, although
577 the defect remains, DL is a better solvent for it, and thereby stabilizes the dissociated monomeric state.
578 With this, it appears as though a small lipid like DL could be considered a chemical that drives
579 disaggregation, analogous to chaotropic denaturants stabilizing the un-folded states of proteins in aqueous
580 solution. Many regulatory molecules in membranes are also small fatty acids; pharmacological agents like
581 general anesthetics, are too small non-polar molecules or atoms. It is possible that these small lipoidal
582 factors act similarly to DL in the problem examined here, and that they preferentially solvate and stabilize
583 the membrane in states where local deformations and defects created by a protein become exposed. This

may promote protein disaggregation, especially at high enough densities, and shift membrane protein equilibria to optimize activity. Altogether, our findings lead to the hypothesis that the complexity of lipid compositions found in biological cell membranes, leveraged through mechanisms such as preferential solvation, permits the cell to regulate and fine-tune the reactions of membrane proteins within – folding, oligomerization, and conformational changes – amidst the extremely variable conditions that life faces. It will be fascinating to continue to unravel the nature of these processes through further experimental and simulation studies.

CONCLUSION

This study provides fundamental insights into an ubiquitous process in membrane physiology, namely protein oligomerization. It also yields a novel perspective of the mechanism by which cells could regulate the stability of membrane protein complexes through subtle variations in the lipid composition of the bilayer. Specifically, we have posited that a principal driving force for the oligomerization of membrane proteins stems from differences in the lipid solvation energetics of the associated and dissociated states. Such differences arise when one of the states in equilibrium introduces a perturbation in the bilayer that would not be naturally observed otherwise, i.e. one that implies a significant free-energy cost from the membrane standpoint. A driving force that originates in the energetics of lipid solvation is by definition highly sensitive to the composition of the membrane. In this regard, the perspective that emerges from this study differs from models that postulate site-specific binding or global changes in the state of the membrane. In our perspective, the lipid bilayer is a system of co-solvents that can alter their spatial distribution so as to preferentially solvate one or more of the states of any given reaction. A particular state might be therefore favored or disfavored, statistically speaking, depending on the energetics of the solvation structure that is achievable by a given co-solvent mixture. It follows that minimal changes in the lipid composition of the membrane can have a profound effect on specific oligomerization reactions, without any global morphological changes that might compromise protein functionality, i.e. what is expected for a physiologically realistic regulatory process.

615 **ACKNOWLEDGEMENTS**

616

617 The Robertson lab is supported by the National Institute of General Medical Science, National Institutes
618 of Health (R01GM120260, R21GM126476); the Faraldo-Gómez lab is funded by the Division of
619 Intramural Research of the National Heart, Lung and Blood Institute, NIH. Access to the NGB30 SANS
620 instrument was provided by the Center for High Resolution Neutron Scattering, a partnership between the
621 National Institute of Standards and Technology and the National Science Foundation under Agreement
622 No. DMR-1508249. This work benefitted from the use of the SasView application, originally developed
623 under NSF award DMR-0520547. SasView contains code developed with funding from the European
624 Union's Horizon 2020 research and innovation program under the SINE2020 project, grant agreement No
625 654000. Computing resources were in part provided by the NIH Supercomputer Biowulf. We thank
626 Kacey Mersch and Tim Lohman for useful discussions during the preparation of this manuscript. The
627 identification of any commercial products or trade names does not imply endorsement or recommendation
628 by the National Institute of Standards and Technology.

629

630 **METHODS**

631

632 ***Coarse-grained molecular dynamics simulations.*** All simulations were calculated with GROMACS 5.2.1
633 (Abraham et al., 2015) using the MARTINI 2.2/ElNeDyn22 forcefield (Wassenaar et al., 2015).
634 Temperature and pressure were maintained constant at 303.15 K and 1 bar, using the velocity-rescale
635 thermostat and the Parrinello-Rahman semi-isotropic barostat, respectively. Equations of motion were
636 integrated using the leapfrog algorithm with a time step of 20 fs. Electrostatics were treated with the
637 reaction field method using a cutoff of 1.2 nm. To ensure statistical significance, several independent runs
638 were performed for each system (see **Fig. 2 – Source Table 1** for further details). The simulations are
639 based on the crystal structure of wild-type CLC-ec1 dimer deposited in the Protein Data Bank, entry 1OTS
640 (resolution 2.51 Å) (Dutzler et al., 2003). Chloride ions were included at sites S_{cen} and S_{int}, and E113
641 (chains A and B) and D417 (chain A) were protonated as indicated from electrostatics analysis (Faraldo-
642 Gómez and Roux, 2004) In the monomer state the N-terminus was truncated up to residue 30, as this
643 cytoplasmic helix, which domain-swaps in the dimer, is highly flexible and able to adopt alternate
644 conformations (Robertson et al., 2010) The atomic structure was coarse-grained using the *martinize* tool;
645 different mixtures of POPE, POPG, DLPE and DLPG lipids were then added around the protein and the

646 systems solvated. The total system charge was neutralized by addition of Na^+ ions, and the system buffered
647 with NaCl to a concentration of 150 mM. The preparatory stages included an 15,000-steps energy
648 minimization using the steepest-descent method, and a 5-ns equilibration to bring the system to desired
649 temperature and pressure. To simplify the visualization and analysis of trajectories, the protein was not
650 permitted to rotate around the Z-axis (i.e. the membrane perpendicular) or to diffuse away from the
651 membrane center. Note this is strictly equivalent to re-defining the laboratory frame as the molecular
652 frame for each snapshot, and thus these restrictions have no impact on the sampling of the internal
653 configurational space. These orientational/translational restraints were implemented with PLUMED
654 (Bonomi et al., 2009); specifically, two centers-of-mass, A and B, were defined using elements of helices
655 H/P (residues 406-409, 411, 412, 194-196, 197, 198) and the linker regions between M/N and E/F
656 (residues 138, 143-145, 347, 348,351-353). In the monomer simulations, harmonic potentials were used
657 to keep both A and B on the YZ plane and equidistant from the membrane center. In the dimer, centers A
658 and B were combined into a single center per monomer, C, and the same restraints were applied to keep
659 the dimer on the YZ plane. The vertical drift of the membrane was also removed prior to trajectory
660 analysis, by re-centering each snapshot so that the midpoint of centers A and B is fixed in place. For the
661 pure bilayer simulations, the same was accomplished by holding fixed the z-component of the membrane
662 center. To map any given descriptor of the lipid structure onto the x-y plane, a grid consisting of square
663 cells each with an area of 0.005 $Å^2$ was constructed. Data derived from analysis of individual lipid
664 molecules in each simulation snapshots were mapped onto specific grid points based on the XY position
665 of the corresponding ester beads (GL1 and GL2); specifically, data was added to all grid points contained
666 within the van der Waals radius of the beads. The grid-point data was then averaged over the all trajectory
667 snapshots. To ascertain which grid-points reflect statistically significant data, the frequency with which
668 each grid point was assigned to any lipid, referred to hereafter as the occupancy number, was annotated.
669 Grid points with less than 40% of the average occupancy were considered to be not statistically significant
670 and excluded from graphical representations and/or global averages. Occupancy numbers were also used
671 to quantify the enrichment of DL lipids in the mixed PO/DL systems, relative to the bulk ratio.
672 Specifically, the percent enrichment at grid point *i* was computed as
673

$$\%E_i = 100\left(\frac{\left[\frac{\rho_{\mathrm{DL}}}{\rho_{\mathrm{PO}}}\right]_i - \left[\frac{\rho_{\mathrm{DL}}}{\rho_{\mathrm{PO}}}\right]_{\mathrm{B}}}{\left[\frac{\rho_{\mathrm{DL}}}{\rho_{\mathrm{PO}}}\right]_{\mathrm{B}}}\right) \quad (1)$$

674

675 where ρ_{DL} and ρ_{PO} refer to the lipid occupancy number, for DLPX and POPX lipids respectively, and the
676 subscripts *i* and B indicates the ratio at grid point *i* or the expected ratio in the bulk given the condition
677 simulated, i.e. if both lipid types were distributed evenly across the box. To compute the enrichment as a
678 function of distance *d* from the protein (or a specific interface), grid points within a mask centered at that
679 distance and 10 Å in width were selected. The percent enrichment was then computed as

680

$$\%E_d = 100\left(\frac{\left[\frac{\rho_{\mathrm{DL}}}{\rho_{\mathrm{PO}}}\right]_{\mathrm{M}} - \left[\frac{\rho_{\mathrm{DL}}}{\rho_{\mathrm{PO}}}\right]_{\mathrm{B}}}{\left[\frac{\rho_{\mathrm{DL}}}{\rho_{\mathrm{PO}}}\right]_{\mathrm{B}}}\right) \quad (2)$$

681

682 where the subscript M refers to the sum of the occupancy numbers over the grid points found within each
683 mask. All grid-based analysis tools are in-house software, available upon request, with the exception of
684 the 3D density maps, which were calculated using the *volmap* plugin of VMD (Humphrey et al., 1996).
685 For more details on the grid-based lipid metrics analysis see **Fig. 2 - Supp. Fig. 2**

686

687 ***Preparation of lipids for reconstitution.*** Detergent solubilized lipids were prepared as described before
688 (Chadda et al., 2016) with the modification that dry lipids were solubilized in 2:1 chloroform:methanol
689 followed by two washes in 3:1 pentane:dichloromethane. This was done due to the fact that DL lipids
690 (DLPE or 12:0 PE; 1,2-dilauroyl-sn-glycero-3-phosphoethanolamine and DLPG or 12:0 PG; 1,2-
691 dilauroyl-sn-glycero-3-phospho-(1'-rac-glycerol) (sodium salt)), unlike PO lipids, were found to be
692 insoluble in chloroform or pentane alone.

693 For a typical preparation, 4 mL of POPE, and 2 mL of POPG (25 mg/mL stocks in chloroform,
694 Avanti Polar Lipids Inc.) were combined in a glass vial (22 mm; RPI, Malvern, PA). The chloroform was
695 evaporated under a continuous stream of 0.22 μm filtered N_2 gas (Ultra High Purity Nitrogen 5.0 Grade;
696 Airgas). The dried lipid mass, was dissolved at least once in 2:1 chloroform/methanol followed by 1-2
697 washes in 3:1 pentane/dichloromethane and drying while rotating, leaving a thin film of lipids along the

698 walls and the bottom of the glass vial. The lipid film, containing 150 mg total lipids (100 mg POPE + 50
699 mg POPG) was dried under continuous stream of N_2, approximately 10-12 minutes. Next, after addition
700 of 161.3 mg (21.5 mg/ml) CHAPS and 7.5 ml Dialysis Buffer (DB: 300 mM KCl, 20 mM citrate pH 4.5
701 (adjusted with NaOH)) sonication was performed leading to a translucent suspension of the
702 CHAPS/POPE/POPG mixture. The final concentration of components was 20 mg/mL 2:1 POPE:POPG
703 (mass ratio) and 35 mM CHAPS. DL lipids were prepared as follows: 40 mg DLPE, and 20 mg DLPG
704 (powder, Avanti Polar Lipids Inc.) were added to a glass vial. The solids were solubilized in 2:1
705 chloroform/methanol and then were taken through the identical washing procedure as PO lipids until a
706 thin, uniform lipid film resulted after drying. Next 64.5 mg CHAPS and 3 mL DB was added followed by
707 sonication. The final concentration of components was 20 mg/mL 2:1 DLPE/DLPG (mass ratio) and
708 CHAPS at 35 mM. Finally, the PO and DL master stocks were mixed in different ratios (volume/volume)
709 resulting in the quaternary lipid mixtures. For instance, to prepare 1 mL of the 20% DL (w/w) lipid
710 mixture, 0.8 mL of the PO lipid stock was mixed with 0.2 mL of the DL lipid stock and used immediately
711 for CLC reconstitution. For reference, the conversion of % DL (w/w) to mole fraction and molality are
712 presented in **Fig. 5 - Source Table 5.**
713
714 ***Differential Scanning Calorimetry (DSC).*** The 2:1 PE/PG - PO and DL 25 mg/mL lipid stocks were solubilized
715 in 2:1 chloroform:methanol as described above, and then mixed together to yield the following titration - 0, 10,
716 30, 50, 70, 90, 100 %DL. After mixing, the lipids were dried under N_2 gas, and solubilized in DB (10-15 mg/mL)
717 by sonication yielding the formation of small unilamellar vesicles. These samples were freeze-thawed 7x to form
718 multi-lamellar vesicles, which were stored at room temperature and examined by DSC days-weeks after
719 preparation. Samples were degassed prior to measurement, and data was collected using a MicroCal VP-DSC
720 differential scanning calorimeter. Data were collected at multiple scan rates to ensure that there was minimal
721 influence of the scan rate on the measured melting transition. Presented data were collected on heating from 2 °C
722 to 50 °C with a scan rate of 30 °C/h and were baseline corrected. Source data is provided in **Fig 3. - Source Table**
723 **1.**
724
725 ***Cryo-EM measurements of liposome size distributions.*** Cryo-electron microscopy (EM) imaging and
726 analysis of images was performed as described earlier (Chadda et al., 2018; Cliff et al., 2019). Briefly,
727 liposomes were freeze-thawed seven times, and then extruded through a 400-nm nucleopore filter (GE
728 Life Sciences) 21 times. 3 μL of the undiluted sample was loaded onto a glow-discharged Lacey carbon

support film (Electron Microscope Sciences), blotted, and plunged into liquid ethane using a Vitrobot System (FEI). Images were collected on a FEI Titan Krios G3 300kV Cryo-TEM microscope with a Gatan K2 Summit Direct electron detector (GATAN). Magnifications of 6500x, 33 000x and 53 000x were used. For size determination, liposomes were manually outlined in Fiji and ImageJ (Schindelin et al., 2012, 2015) to measure the outer radii of all liposomes, including those located on the carbon. Multilamellarity was manually counted as the fraction of vesicles containing more than one bilayer. Liposome size distribution source data is provided in **Fig. 3 - Source Table 2.**

Small-angle neutron scattering (SANS) experiments. Liposomes were prepared by drying as described previously, then sonicating the dried lipid films in reconstitution buffer prepared with 99.9% pure D_2O (Cambridge Isotopes). Note, the *pD* of the buffer was adjusted by soaking the *pH* electrode in pure D_2O for several minutes and then adjusted with NaOH. Following $pD = pH_{measured} + 0.33$ (Krężel and Bal, 2004), we adjusted the solution to 4.17 for a final *pD* of 4.5. Prior to measurement, liposomes were freeze-thawed following the procedure described previously, then extruded in two steps, first through 400 nm filters and then through 100 nm nucleopore membranes.

SANS data were collected on the NGB30SANS instrument at the NIST Center for Neutron Research at the National Institute of Standards and Technology (NIST). Data were collected using a neutron wavelength (λ) 6 Å and a wavelength spread ($\Delta\lambda/\lambda$) of 0.12 with sample to detector distances of 1 m, 4 m, and 13 m. Additional data were collected using $\lambda = 8.4$ Å with a sample to detector distance of 13 m. These instrument configurations provided access to a q-range of $0.001\ Å^{-1} < q < 0.04\ Å^{-1}$ where q is the scattering vector and is defined as $q = 4\pi\lambda^{-1}\sin(\theta/2)$ and θ is the scattering angle. Samples were sealed in titanium cells with quartz windows and sample temperature was controlled at 25 °C (± 0.1 °C) during data acquisition. Data were reduced to absolute intensity using the macros provided by NIST (Kline, 2006).

SANS data were analyzed with the multilamellar form factor in the SasView application. The data showed a broad shoulder at $q \approx 0.06\ Å^{-1}$ due to the presence of a mixture of unilamellar and multilamellar vesicles (Scott et al., 2019). SANS data were fit with an array distribution of N, where N is the number of lamellar shells and the reported results are for the distribution that gave the best fit to the data, defined as the minimum χ^2 value. Approximately 85- 90% of the vesicle population contained a single lamella which was in good agreement with Cryo-EM experiments that confirmed the presence of ≈ 85% unilamellar, ≈

759 10% bi-lamellar (vesicles containing 2 bilayers) and ≈ 5% multilamellar vesicles (vesicles with 3 or more
760 bilayers).
761 Cryo-EM imaging of the liposomes also showed a bimodal distribution of vesicle sizes. The SANS
762 analysis fixed the distribution of outer vesicle radii based on the cryo-EM results and only fit the data for
763 $q > 0.015$ Å^{-1} where the form factor contribution from the vesicle radii were constant (Pencer et al., 2006).
764 The parameters fit during the analysis were the bilayer thickness (d_b), the water layer thickness (d_w) and
765 the scattering length density of the bilayer (results not shown). Source data is provided in **Fig. 3 - Source**
766 **Table 3.**
767
768 ***Protein purification, labeling, and reconstitution.*** DNA constructs for CLC-ec1 C85A/H234C (WT),
769 C85A/H234C/I201W/I422W (WW) (Chadda et al., 2016) and C85A/H234C/R230C/L249C (RCLC) were
770 described previously (Chadda et al., 2018). Expression and purification of these CLC-ec1 variants was
771 carried out as described earlier (Chadda et al., 2016). Briefly, proteins were overexpressed in BL21-AI
772 *E.coli* competent cells and extracted into 2% n-Decyl-β-D-Maltopyranoside (DM; Anatrace, Maumee
773 OH) containing 5 mM TCEP (Tris(2-carboxyethyl)phosphine; Soltec Bioscience, Beverly, MA). After
774 removing cellular debris by centrifugation, the protein was affinity purified using TALON cobalt affinity
775 resin (Clontech Laboratories, Mountain View, CA) followed by size exclusion chromatography on
776 Superdex 200 10/30 GL size exclusion column (GE Healthcare, Little Chalfont, UK) into size exclusion
777 buffer (SEB): 150 mM NaCl, 20 mM MOPS pH 7.0, 5 mM analytical-grade DM.
778 Addition of TCEP during purification ensures that the engineered cysteine at the residue H234C
779 remains reduced and available for maleimide labeling. This can be quantitatively estimated after reacting
780 the purified protein with Ellman's reagent (DNTB, 5,5'-Dithio-bis(2-nitrobenzoic acid); Sigma-Aldrich)
781 as described before (Chadda et al., 2016). Fluorescent labeling of the protein is conducted in presence of
782 5X Cy5-maleimide followed by separation of unreacted dye using affinity and size-exclusion
783 chromatography. Quantification of the Cy5 labeling yield per subunit, P_{Cy5}, was carried out as described
784 previously (Chadda et al., 2016; Chadda and Robertson, 2016).
785 For reconstitution, Cy5-labeled protein is mixed 20 mg/mL lipids in DB + 35 mM CHAPS and
786 then dialyzed in independent buckets to prevent the possibility of cross-contamination between different
787 lipid compositions. Note, the effect of contamination during dialysis appears negligible in our
788 experiments, as we quantified it by photobleaching analysis and observed a small, non-significant
789 difference (**Figure 5 - Figure Supplement 1E**).

790

791 ***Functional measurements.*** Chloride transport assays from 400 nm extruded liposomes were performed
792 as described earlier (Walden et al., 2007; Chadda et al., 2016). Functional measurements were carried out
793 6.4 ± 6.1 days (mean ± std, n = 2-5) after freeze/thaw and sample incubation in the dark, at room
794 temperature. All data is listed in **Figure 4 - Source Table 1**.

795

796 ***Single-molecule photobleaching analysis and calculations of dimerization.*** Proteoliposomes samples
797 were extruded, imaged on TIRF microscope, and the videos analyzed for counting single-molecule
798 photobleaching steps as described earlier (Chadda et al., 2016; Chadda and Robertson, 2016; Chadda et
799 al., 2018). Briefly, dialyzed proteoliposomes were freeze-thawed seven times leading to formation of large
800 multilamellar vesicles (MLVs). The samples were stored at room temperature, in the dark, with 0.02%
801 NaN_3 until extrusion and single-molecule imaging. Overall, the Cy5 labeling yield was P_{Cy5} = 0.66 ±
802 0.00 (mean ± sem, n = 27) for wild-type CLC-ec1 samples. Imaging was carried out 3-15 days after
803 freeze-thaw and sample incubation in the dark, at room temperature. Images were analyzed as described
804 previously using the *imscroll* software in MATLAB (Friedman and Gelles, 2015).

805 To quantify the underlying dimerization reaction from the photobleaching data, the same methods
806 described in were followed (Chadda et al., 2016; Chadda and Robertson, 2016; Chadda et al., 2018).
807 Briefly, photobleaching probability distributions (P_1, P_2, P_{3+}) were determined for each construct as a
808 function of protein density and lipid composition. The fraction of dimer in the protein population, F_{Dimer},
809 was estimated by least-squares fitting of the linear combination of the probability distributions for the
810 monomer and dimer controls under similar conditions. Equilibrium constants were obtained by fitting the
811 data to an equilibrium dimerization isotherm,

812

$$F_{Dimer} = \frac{1 + 4K_{eq}\chi^* - \sqrt{1 + 8K_{eq}\chi^*}}{4K_{eq}\chi^*} \quad (3)$$

813

814 and then converted to $\Delta G° = -RTln(K_{eq})$, standard state = 1 subunit/lipid. All data is listed in **Fig. 5 -**
815 **Source Tables 1-7**.

816

817

818

REFERENCES

Abraham, M.J., T. Murtola, R. Schulz, S. Páll, J.C. Smith, B. Hess, and E. Lindahl. 2015. GROMACS: High performance molecular simulations through multi-level parallelism from laptops to supercomputers. *Softwarex*. 1:19–25. doi:10.1016/j.softx.2015.06.001.

Aleksandrova, A.A., E. Sarti, and L.R. Forrest. 2019. MemSTATS: A Benchmark Set of Membrane Protein Symmetries and Pseudo-Symmetries. *J Mol Biol*. 432:597–604. doi:10.1016/j.jmb.2019.09.020.

Andersen, O.S., and R.E.K. II. 2007. Bilayer Thickness and Membrane Protein Function: An Energetic Perspective. *Biophysics Biomol Struct*. 36:107–130. doi:10.1146/annurev.biophys.36.040306.132643.

Anselmi, C., K.M. Davies, and J.D. Faraldo-Gómez. 2018. --Mitochondrial ATP synthase dimers spontaneously associate due to a long-range membrane-induced force. *J Gen Physiology*. 150:763–770. doi:10.1085/jgp.201812033.

Bonomi, M., D. Branduardi, G. Bussi, C. Camilloni, D. Provasi, P. Raiteri, D. Donadio, F. Marinelli, F. Pietrucci, R.A. Broglia, and M. Parrinello. 2009. PLUMED: A portable plugin for free-energy calculations with molecular dynamics. *Comput Phys Commun*. 180:1961–1972. doi:10.1016/j.cpc.2009.05.011.

Botelho, A.V., T. Huber, T.P. Sakmar, and M.F. Brown. 2006. Curvature and Hydrophobic Forces Drive Oligomerization and Modulate Activity of Rhodopsin in Membranes. *Biophys J*. 91:4464–4477. doi:10.1529/biophysj.106.082776.

Brown, M.F. 2017. Soft Matter in Lipid-Protein Interactions. *Annu Rev Biophys*. 46:379–410. doi:10.1146/annurev-biophys-070816-033843.

Brügger, B. 2014. Lipidomics: analysis of the lipid composition of cells and subcellular organelles by electrospray ionization mass spectrometry. *Annu Rev Biochem*. 83:79–98. doi:10.1146/annurev-biochem-060713-035324.

Chadda, R., L. Cliff, M. Brimberry, and J.L. Robertson. 2018. A model-free method for measuring dimerization free energies of CLC-ec1 in lipid bilayers. *J Gen Physiology*. 150:355–365. doi:10.1085/jgp.201711893.

Chadda, R., V. Krishnamani, K. Mersch, J. Wong, M. Brimberry, A. Chadda, L. Kolmakova-Partensky, L.J. Friedman, J. Gelles, and J.L. Robertson. 2016. The dimerization equilibrium of a ClC Cl(-)/H(+) antiporter in lipid bilayers. *Elife*. 5:e17438. doi:10.7554/elife.17438.

Chadda, R., and J.L. Robertson. 2016. Measuring Membrane Protein Dimerization Equilibrium in Lipid Bilayers by Single-Molecule Fluorescence Microscopy. *Methods Enzymol*. 581:53–82. doi:10.1016/bs.mie.2016.08.025.

Cliff, L., R. Chadda, and J.L. Robertson. 2019. Occupancy distributions of membrane proteins in heterogeneous liposome populations. *Biochimica Et Biophysica Acta Biomembr*. 1862:183033. doi:10.1016/j.bbamem.2019.183033.

Corradi, V., E. Mendez-Villuendas, H.I. Ingólfsson, R.-X. Gu, I. Siuda, M.N. Melo, A. Moussatova, L.J. DeGagné, B.I. Sejdiu, G. Singh, T.A. Wassenaar, K.D. Magnero, S.J. Marrink, and D.P. Tieleman. 2018. Lipid-Protein Interactions Are Unique Fingerprints for Membrane Proteins. *Acs Central Sci*. 4:709–717. doi:10.1021/acscentsci.8b00143.

Dutzler, R., E.B. Campbell, M. Cadene, B.T. Chait, and R. MacKinnon. 2002. X-ray structure of a ClC chloride channel at 3.0 Å reveals the molecular basis of anion selectivity. *Nature*. 415:287–294. doi:10.1038/415287a.

Dutzler, R., E.B. Campbell, and R. MacKinnon. 2003. Gating the Selectivity Filter in ClC Chloride Channels. *Science*. 300:108–112. doi:10.1126/science.1082708.
Faraldo-Gómez, J.D., and B. Roux. 2004. Electrostatics of Ion Stabilization in a ClC Chloride Channel Homologue from Escherichia coli. *J Mol Biol*. 339:981–1000. doi:10.1016/j.jmb.2004.04.023.
Fricke, H. 1925. THE ELECTRIC CAPACITY OF SUSPENSIONS WITH SPECIAL REFERENCE TO BLOOD. *J Gen Physiology*. 9:137–152. doi:10.1085/jgp.9.2.137.
Friedman, L.J., and J. Gelles. 2015. Multi-wavelength single-molecule fluorescence analysis of transcription mechanisms. *Methods San Diego Calif*. 86:27–36. doi:10.1016/j.ymeth.2015.05.026.
Goodall, M.C. 1971. Thickness dependence in the action of Gramicidin A on lipid bilayers. *Arch Biochem Biophys*. 147:129–135. doi:10.1016/0003-9861(71)90318-3.
Humphrey, W., A. Dalke, and K. Schulten. 1996. VMD: Visual molecular dynamics. *J Mol Graphics*. 14:33–38. doi:10.1016/0263-7855(96)00018-5.
Kahraman, O., and C.A. Haselwandter. 2019. Supramolecular organization of membrane proteins with anisotropic hydrophobic thickness. *Soft Matter*. 15:4301–4310. doi:10.1039/c9sm00358d.
Kline, S.R. 2006. Reduction and analysis of SANS and USANS data using IGOR Pro. *J Appl Crystallogr*. 39:895–900. doi:10.1107/s0021889806035059.
Krężel, A., and W. Bal. 2004. A formula for correlating pKa values determined in D2O and H2O. *J Inorg Biochem*. 98:161–166. doi:10.1016/j.jinorgbio.2003.10.001.
Kučerka, N., M.-P. Nieh, and J. Katsaras. 2011. Fluid phase lipid areas and bilayer thicknesses of commonly used phosphatidylcholines as a function of temperature. *Biochim Biophys Acta*. 1808:2761–71. doi:10.1016/j.bbamem.2011.07.022.
Lee, J.C., and S.N. Timasheff. 1981. The stabilization of proteins by sucrose. *J Biological Chem*. 256:7193–201.
Li, Y., X. Zhang, and D. Cao. 2013. The role of shape complementarity in the protein-protein interactions. *Sci Rep-uk*. 3:3271. doi:10.1038/srep03271.
Maduke, M., D.J. Pheasant, and C. Miller. 1999. High-Level Expression, Functional Reconstitution, and Quaternary Structure of a Prokaryotic Clc-Type Chloride Channel. *J Gen Physiol*. 114:713–722. doi:10.1085/jgp.114.5.713.
Marr, A.G., and J.L. Ingraham. 1962. EFFECT OF TEMPERATURE ON THE COMPOSITION OF FATTY ACIDS IN ESCHERICHIA COLI. *J Bacteriol*. 84:1260–7.
Marsh, D. 1995. Preferential solvation and the selectivity of lipid-protein interactions. *Biophys J*. 69:1191–1192. doi:10.1016/s0006-3495(95)79993-3.
Meer, G. van, D.R. Voelker, and G.W. Feigenson. 2008. Membrane lipids: where they are and how they behave. *Nat Rev Mol Cell Biology*. 9:112–24. doi:10.1038/nrm2330.
Mobashery, N., C. Nielsen, and O.S. Andersen. 1997. The conformational preference of gramicidin channels is a function of lipid bilayer thickness 1. *Febs Lett*. 412:15–20. doi:10.1016/s0014-5793(97)00709-6.
Mondal, S., G. Khelashvili, J. Shan, O.S. Andersen, and H. Weinstein. 2011. Quantitative modeling of membrane deformations by multihelical membrane proteins: application to G-protein coupled receptors. *Biophys J*. 101:2092–101. doi:10.1016/j.bpj.2011.09.037.
Mondal, S., G. Khelashvili, and H. Weinstein. 2014. Not Just an Oil Slick: How the Energetics of Protein-Membrane Interactions Impacts the Function and Organization of Transmembrane Proteins. *Biophys J*. 106:2305–16. doi:10.1016/j.bpj.2014.04.032.
Nguitragool, W., and C. Miller. 2007. CLC Cl-/H+ transporters constrained by covalent cross-linking. *Proc National Acad Sci*. 104:20659–20665. doi:10.1073/pnas.0708639104.

Pan, J., D. Marquardt, F.A. Heberle, N. Kučerka, and J. Katsaras. 2014. Revisiting the bilayer structures of fluid phase phosphatidylglycerol lipids: Accounting for exchangeable hydrogens. *Biochim Biophys Acta*. 1838:2966–9. doi:10.1016/j.bbamem.2014.08.009.

Pencer, J., S. Krueger, C.P. Adams, and J. Katsaras. 2006. Method of separated form factors for polydisperse vesicles. *J Appl Crystallogr*. 39:293–303. doi:10.1107/s0021889806005255.

Phillips, R. 2018. Physics of Biological Membranes. 73–105. doi:10.1007/978-3-030-00630-3_3.

Record, M.T., and C.F. Anderson. 1995. Interpretation of preferential interaction coefficients of nonelectrolytes and of electrolyte ions in terms of a two-domain model. *Biophys J*. 68:786–794. doi:10.1016/s0006-3495(95)80254-7.

Robertson, J.L., L. Kolmakova-Partensky, and C. Miller. 2010. Design, function and structure of a monomeric ClC transporter. *Nature*. 468:844–7. doi:10.1038/nature09556.

Sanders, C.R., and K.F. Mittendorf. 2011. Tolerance to changes in membrane lipid composition as a selected trait of membrane proteins. *Biochemistry-us*. 50:7858–67. doi:10.1021/bi2011527.

Schellman, J.A. 1987. Selective binding and solvent denaturation. *Biopolymers*. 26:549–559. doi:10.1002/bip.360260408.

Schellman, J.A. 2003. Protein Stability in Mixed Solvents: A Balance of Contact Interaction and Excluded Volume. *Biophys J*. 85:108–125. doi:10.1016/s0006-3495(03)74459-2.

Schindelin, J., I. Arganda-Carreras, E. Frise, V. Kaynig, M. Longair, T. Pietzsch, S. Preibisch, C. Rueden, S. Saalfeld, B. Schmid, J.-Y. Tinevez, D.J. White, V. Hartenstein, K. Eliceiri, P. Tomancak, and A. Cardona. 2012. Fiji: an open-source platform for biological-image analysis. *Nat Methods*. 9:676–82. doi:10.1038/nmeth.2019.

Schindelin, J., C.T. Rueden, M.C. Hiner, and K.W. Eliceiri. 2015. The ImageJ ecosystem: An open platform for biomedical image analysis. *Mol Reprod Dev*. 82:518–29. doi:10.1002/mrd.22489.

Scott, H.L., A. Skinkle, E.G. Kelley, M.N. Waxham, I. Levental, and F.A. Heberle. 2019. On the Mechanism of Bilayer Separation by Extrusion, or Why Your LUVs Are Not Really Unilamellar. *Biophys J*. 117:1381–1386. doi:10.1016/j.bpj.2019.09.006.

Tanford, C. 1969. Extension of the theory of linked functions to incorporate the effects of protein hydration. *J Mol Biol*. 39:539–544. doi:10.1016/0022-2836(69)90143-0.

Tanford, C. 1978. The hydrophobic effect and the organization of living matter. *Science*. 200:1012–1018. doi:10.1126/science.653353.

Timasheff, S.N. 2002. Protein Hydration, Thermodynamic Binding, and Preferential Hydration. *Biochemistry-us*. 41:13473–13482. doi:10.1021/bi020316e.

Valentine, D.L. 2007. Adaptations to energy stress dictate the ecology and evolution of the Archaea. *Nat Rev Microbiol*. 5:316–323. doi:10.1038/nrmicro1619.

Walden, M., A. Accardi, F. Wu, C. Xu, C. Williams, and C. Miller. 2007. Uncoupling and Turnover in a Cl−/H+ Exchange Transporter. *J Gen Physiology*. 129:317–329. doi:10.1085/jgp.200709756.

Wassenaar, T.A., H.I. Ingólfsson, R.A. Böckmann, D.P. Tieleman, and S.J. Marrink. 2015. Computational Lipidomics with insane : A Versatile Tool for Generating Custom Membranes for Molecular Simulations. *J Chem Theory Comput*. 11:2144–2155. doi:10.1021/acs.jctc.5b00209.

950 **FIGURES**
951

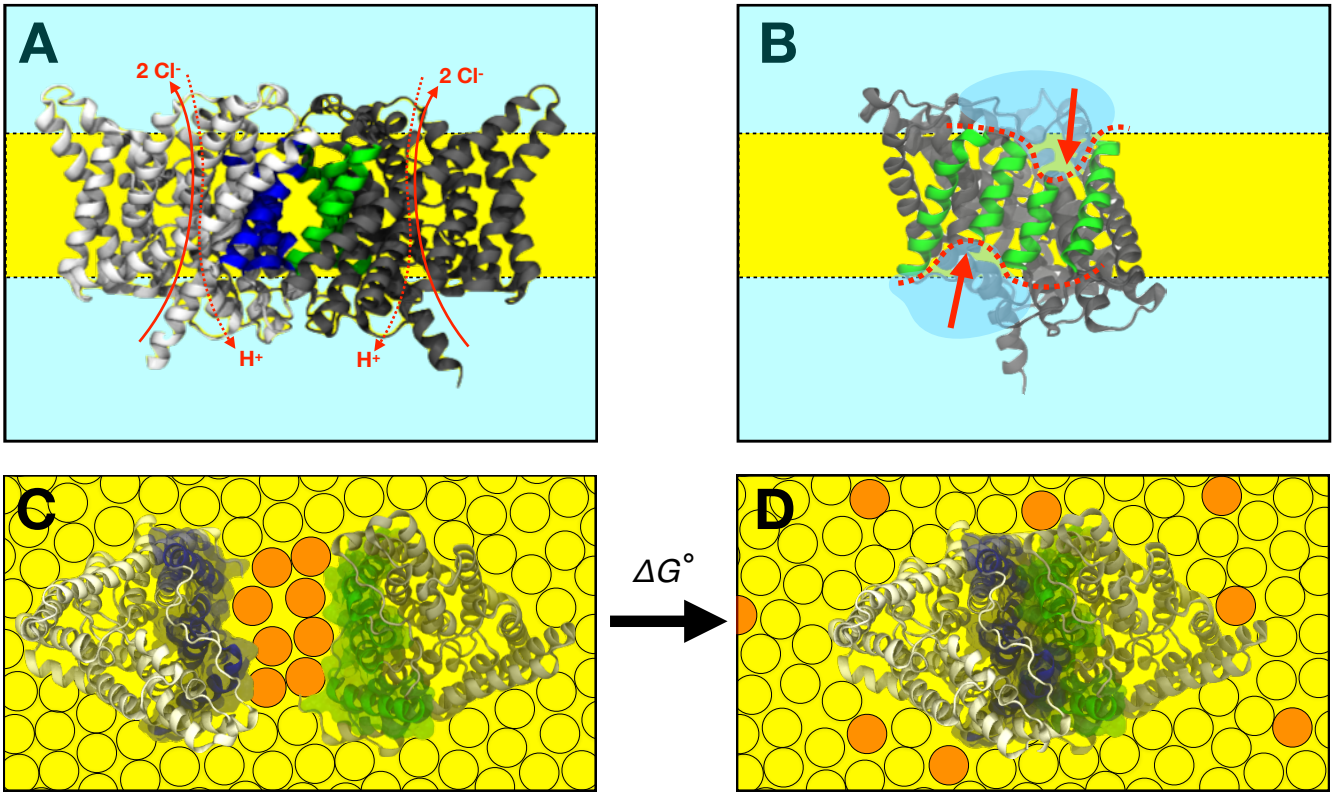

Figure 1. The CLC-ec1 dimerization reaction in lipid bilayers. (A) Side view of the CLC-ec1 homodimer in the lipid bilayer. Two subunits shown in silver and grey, with helices forming the dimerization interface highlighted blue and green. The hydrophobic core of the membrane is depicted in yellow. Approximate pathways for Cl^- and H^+ transport is shown with red arrows. (B) The dimerization interface of the monomer. The four helices forming the interface (Q, P, H & I) are shown in green, with red dotted line and arrows highlighting the shorter H & P helices at the center of the interface. (C,D) Top view of dissociated and associated end-points of the CLC-ec1 dimerization reaction, with the free energy of dimerization defined as ΔG°. Circles represent lipids, with orange circles highlighting and example set of lipids that exchange between the dimerization interface and the bulk upon dimerization.

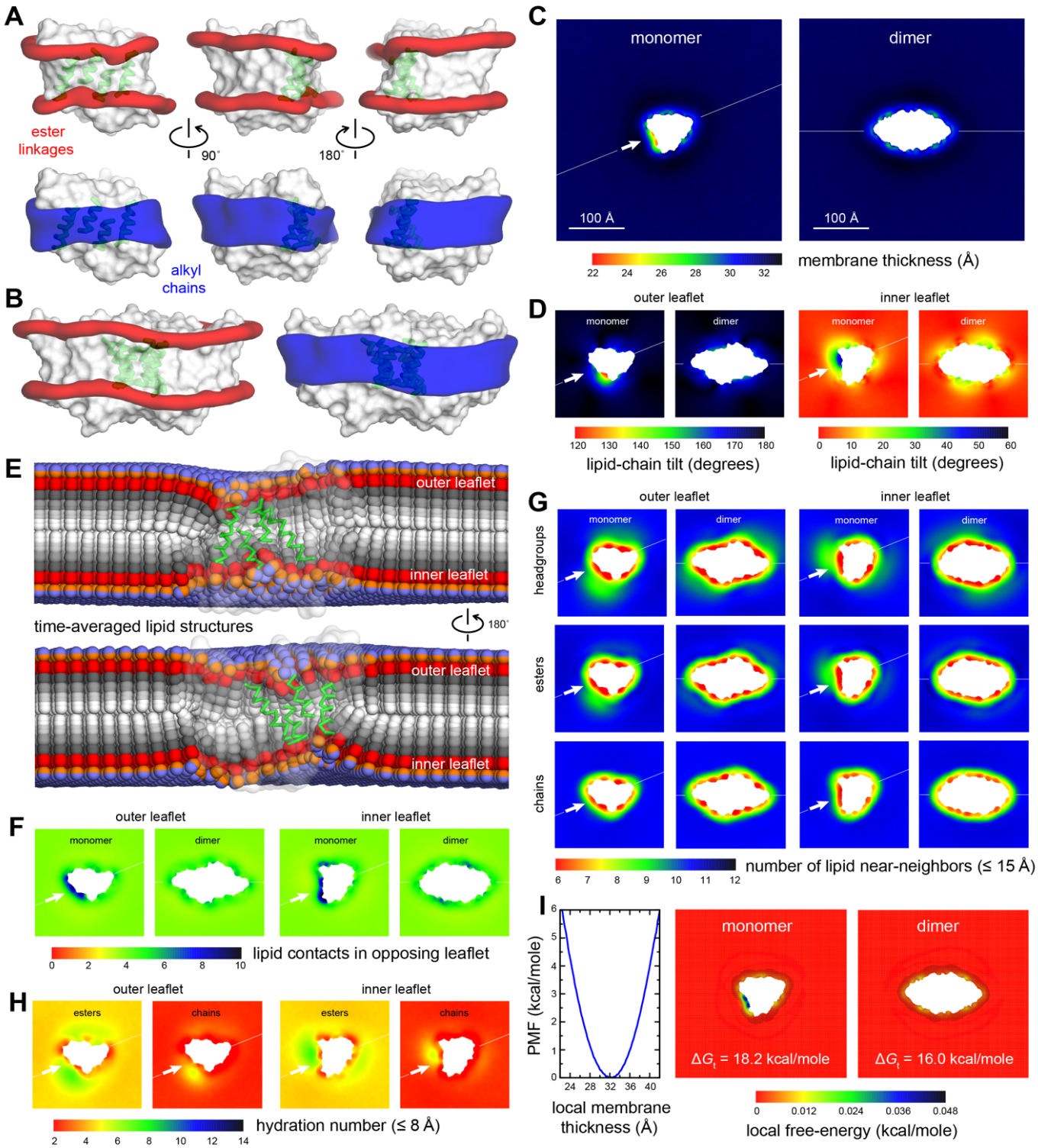

Figure 2. Membrane morphology around CLC-ec1 monomer and dimer from molecular dynamics simulations. *Continued on next page ...*

Figure 2. Membrane morphology around CLC-ec1 monomer and dimer from molecular dynamics simulations. Results are shown for 2:1 POPE:POPG membranes, averaging 8 independent trajectories of ≈ 7.5 μs each for the monomer, and 10 trajectories of ≈ 10 μs each for the dimer (**Fig. 2 – Source Table 1**). All simulations are based on the coarse-grained MARTINI force field. (A, B) 3D density maps for the ester linkages (red) or alkyl chains (blue) in the vicinity (≤ 10 Å) of the protein (white surface), for (A) the monomer and (B) the dimer. In (A), 3 different views of the lipid first-shell are depicted; the 4 helices at dimerization interface are highlighted (green). (C-H) Spatially resolved grid-based analysis of different descriptors of the lipid bilayer structure. See **Fig. 2 – Fig. Supp. 2** for details. (C) 2D maps of the local bilayer thickness across the simulation system. The proteins occupy the central area (white mask). Note monomer and dimer are oriented differently. To facilitate this comparison an axis perpendicular to the dimerization interface (white arrow) is drawn in both cases. (D) Variation in the mean lipid tilt-angle across the system, relative to the bilayer perpendicular, for both the outer and inner leaflets. (E) Time-averaged lipid conformations mapped onto a 2D grid. Alkyl chains (gray scale), ester linkages (red), and headgroups (orange/purple) are shown as spheres. Note perfectly isotropic dynamics, when time-averaged, results in a linear structure for the entire molecule. Data is shown for the monomer only (transparent surface), viewed from two sides. The 4 helices at the dimerization interface are highlighted (green). (F) Number of contacts formed by the alkyl-chains in one leaflet with those in the opposing leaflet, per chain and time-averaged. (G) Variation in the number of lipid neighbors within a fixed distance, at the level of the phosphates, esters or alkyl chains layers. (H) Number of water contacts with beads from either the esters or alkyl chains, referred to as "hydration number". (I) Analysis of the free-energy cost of the thickness perturbation shown in panel (C). On the left, free energy as a function of the Z-distance between the ester groups in directly opposing lipid molecules in either leaflet, based on simulations of a pure 2:1 POPE:POPG membrane. On the right, the 2D maps in panel (C) are translated into free-energy maps using the PMF curve as well as data mapping the mean lipid molecule number in each region. Data is shown for the dimer and the monomer. The energetic penalty associated with solvating thickness deformations around the protein is integrated over the shaded masked region (< 10 Å from protein) with ΔG_t (monomer) = 18.2 kcal/mole and ΔG_t (dimer) = 16.0 kcal/mole. The resulting membrane thickness contribution of the free energy gained upon burying the dimerization interface upon association is $\Delta\Delta G_t = \Delta G_t$ (dimer) – 2 × ΔG_t (monomer) = -20.4 kcal/mole. See **Fig. 2 - Fig. Supp. 1-3**, **Source Table 1** for additional details.

953

954

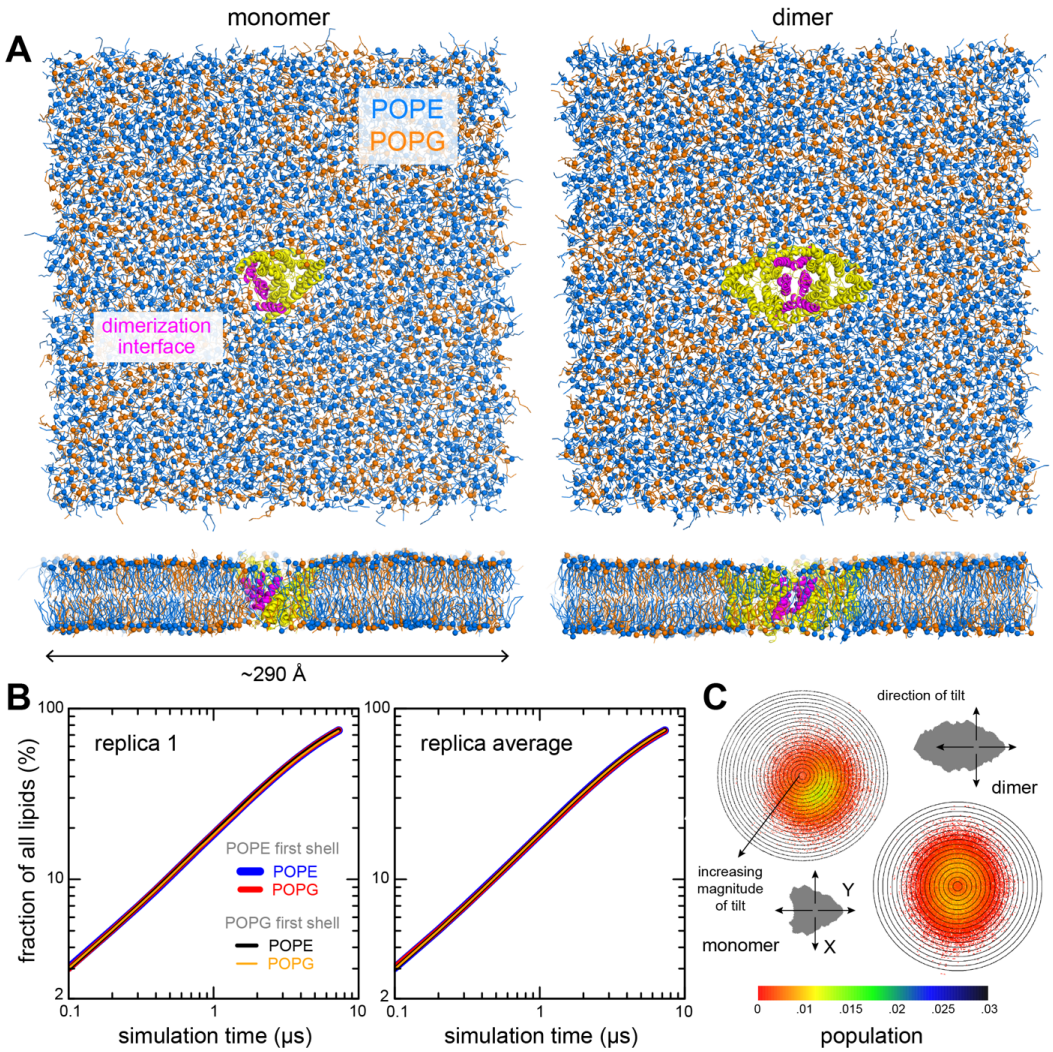

Figure 2 – Figure Supplement 1. Simulation systems and quantification of configurational lipid and protein sampling. (A) Simulation systems for the CLC-ec1 monomer (left) and dimer (right) in 2:1 POPE (blue):POPG (orange) lipid bilayer. The protein is shown as yellow helices, with the dimerization interface highlighted in magenta. The systems include a total of 2,784 and 2,773 lipid molecules, respectively. (B) Evaluation of the degree of lipid mixing for the monomer system. For any lipid *i*, we quantify, as a function of simulation time, the percentage of all other lipids *j* in the same leaflet that reside for at least 3 ns in a 10-Å shell around lipid *i.* Results are shown for a single trajectory (left), and for the average of all trajectories (right). At any given time, the number of lipids *j* in these shells is, on average, about 6. Results are shown for a single trajectory, and for the average of all trajectories. (C) Evaluation of the protein tilt, relative to the membrane perpendicular (Z-axis). Data for the isolated monomer is compared with the monomer in the context of the dimer. The polar plots describe the magnitude of the tilt in the radial coordinate, contoured in 1º increments; and the XY direction of tilt in the angular coordinate, as indicated. These descriptors were evaluated as a function of simulation time for all trajectories and represented here as probability distributions (color bar). The direction and magnitude of tilt derive from evaluation of a vector connecting two centers within the protein, C_1 and C_2, each defined by a set of backbone beads (324, 327, 332, 361, 370, 413 for C_1; and residues 202, 267, 272, 363, 402, 446 for C_2), identical for the monomer and dimer systems .In the context of the dimer, the monomer fluctuates around the membrane perpendicular, as can be expected for a symmetric dimer, preferring a tilt of ≈ 4º; when isolated, the preferred tilt increases slightly, ≈ 7º, and the fluctuations are no longer centered on the membrane perpendicular. In both cases, the probability distributions appear to be fully defined, indicating near complete sampling of the accessible orientation space.

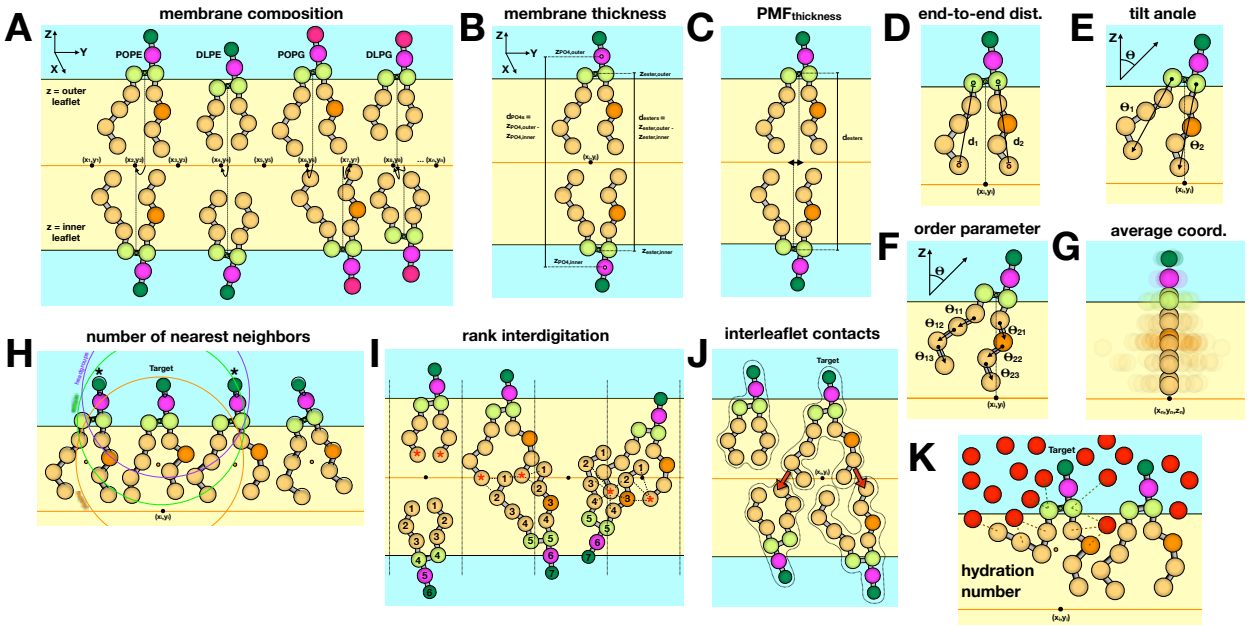

Figure 2 – Figure Supplement 2. Schematic of different descriptors of lipid-bilayer structure. (A) Composition of membranes simulated in this study. All simulations maintain a 2:1 PE:PG ratio for the lipid headgroups, while varying the DL:PO acyl-chain composition. The coarse-grained particles or beads used to represent each lipid molecule are shown as spheres. Analysis is typically performed for each leaflet (outer vs. inner) unless otherwise noted. For each simulation snapshot and each trajectory, a one-to-one assignment of each lipid molecule (or specific groups therein) to a point in a 2-dimensional grid on the membrane XY plane is made. For each lipid, the descriptor of interest is calculated on the basis of the 3D coordinates of the system in that snapshot/trajectory, and assigned to the corresponding grid-point. Finally, all values mapped onto each grid point are averaged for all snapshots/trajectories, and represented as a color-coded 2D map. (B) To calculate the membrane thickness, the mean Z-coordinate of either the phosphate or the ester layer is calculated for each leaflet, and mapped onto 2D grids as mentioned above; the mean Z-coordinate map for the inner leaflet is the subtracted from that of the outer leaflet, in the regions of the grid where both are defined. (C) For the potential of mean force (PMF) calculations, the membrane distance is determined by the ester bead distance between the nearest lipids to the central grid point in the opposing leaflets. (D) Acyl chain end-to-end distance, $d_{ester\text{-}Cn}$, where n represents the last bead in the acyl chain (n = 4 for PO lipids). (E) Lipid tilt angle, $\boldsymbol{\Theta}_i$, for each chain i relative to the membrane normal (Z-axis). (F) Mean order parameter calculated along all acyl-chain bond angles, $\boldsymbol{\Theta}_{ij}$, across chain i and bond j. (G) The average lipid structure for a point on the 2D grid is calculated by averaging the 3D coordinates of the lipid molecules assigned to that point. (H) To evaluate the number of nearest neighbors j for a given lipid i, a set of geometric centers are defined for either the headgroup, ester groups, or acyl chains in both i and j. Lipid j is considered to be a neighbor of i if the distance between the respective centers is 15 Å or less. (I) To rank the degree of interdigitation of a given alkyl chain i with all other lipids j in the opposing leaflet, the beads in j are indexed as indicated, and those within 6 Å of the last bead in i (marked by asterisk) are identified; the rank averaged over these contacts and time is reported. (J) Interleaflet contacts are the total number of contacts formed between each alkyl chain I and beads in any chain j in the opposing leaflet where a contact requires the beads be within 6 Å of each other. (K) The degree of hydration is quantified for each lipid molecule, either for the ester layer or the alkyl chains, as the total number of lipid-water contacts where a contact is counted if the CG water is within 8 Å of a bead in the selected group.

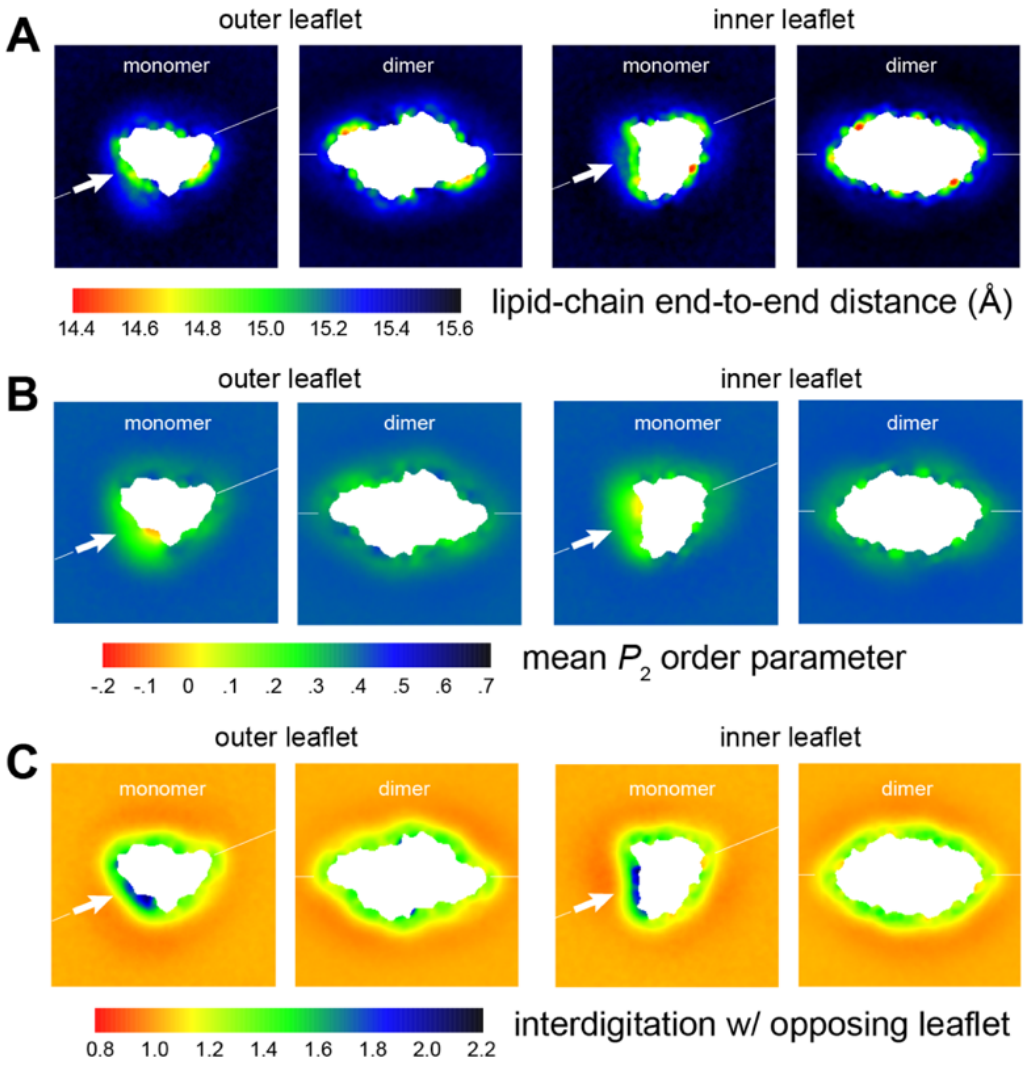

Figure 2 – Figure Supplement 3. Membrane morphology around CLC-ec1 monomer and dimer from molecular dynamics simulations. Note monomer and dimer are oriented differently. To facilitate this comparison an axis perpendicular to the dimerization interface (white arrow) is drawn in both cases. (A) Variation in the end-to-end distance in the lipid alkyl-chains across the simulation system, for both outer and inner leaflet. (B) Variation in the second-rank order parameter, P_2, of the coarse-grained C-C bonds in the alkyl-chains. The P_2 parameter of a given C-C bond is defined as 1/2 (3 $\cos^2\langle\theta\rangle - 1$), where $\langle\theta\rangle$ denotes the ensemble-average value of the angle formed by the bond and the bilayer perpendicular (Z-axis). The plots show the mean value of P_2 for the three C-C bonds in the PO lipids, mapped across the system. (C) Interdigitation rank for the alkyl-chains in one leaflet with the alkyl-chains in the opposing leaflet. See **Figure 2 – Figure Supplement 2** for further details.

957
958
959

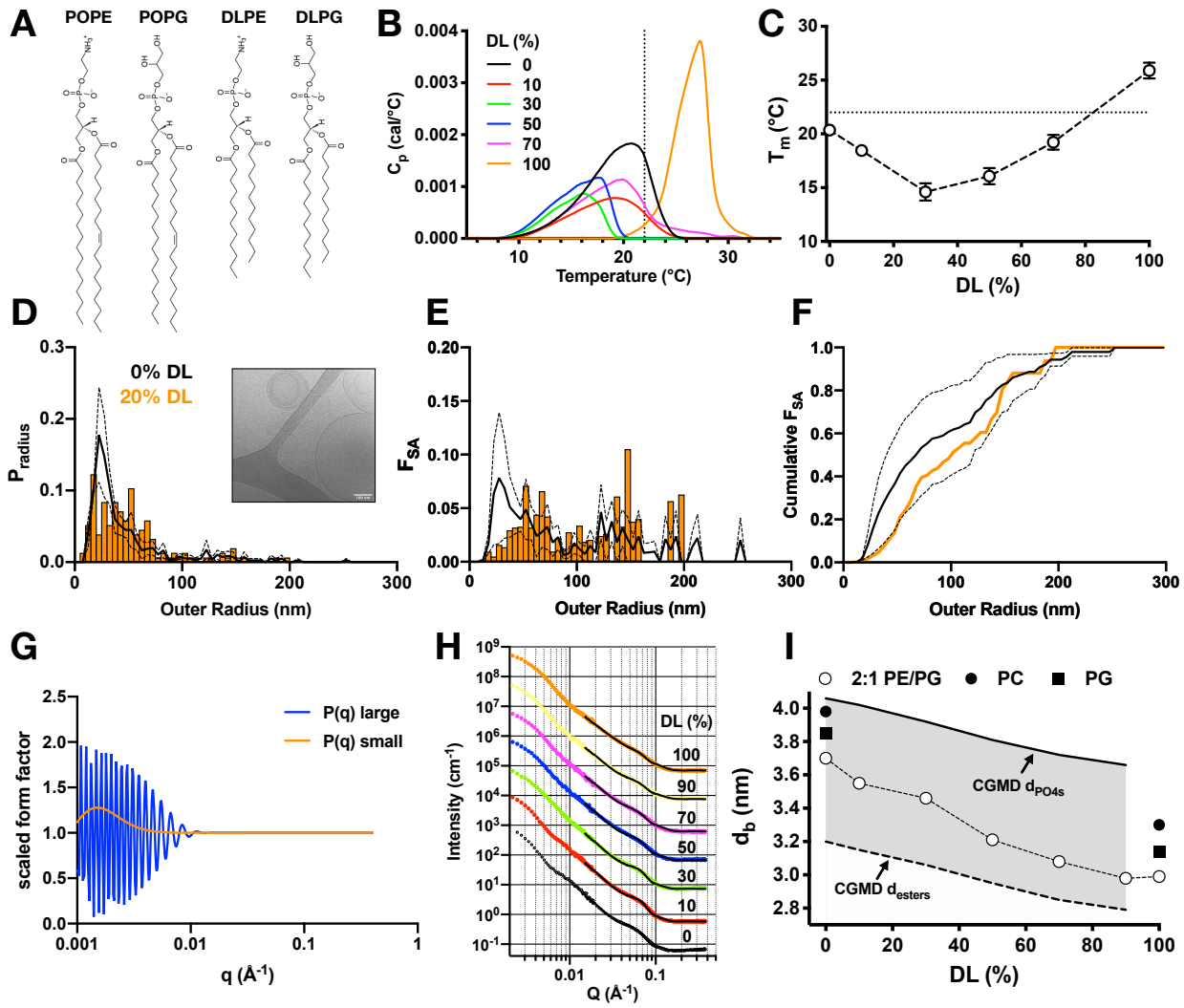

Figure 3. Physical properties of 2:1 PE:PG membranes with mixed DL/PO acyl chains. (A) Chemical structures of lipids POPE, POPG, DLPE and DLPG. (B) Differential scanning calorimetry (DSC) thermograms of DL/PO mixed membranes in the multilamellar vesicle state. Dotted line marks approximate ambient room temperature (RT) of 22°C. (C) Peak phase transition temperature, T_m, as a function of % DL, dotted line indicates RT. (D) Liposome size distribution of 20% DL liposomes (orange histogram), extruded through 400 nm filters and imaged by cryo-electron microscopy (inset). Black line shows mean ± standard deviation distribution of 400 nm extruded 2:1 POPE:POPG vesicles (Cliff et al., 2019). (E) Distribution of the fractional surface area of each liposome composition. (G) Cumulative surface area distributions. (G) Multilamellar spherical form factors for small (orange) and large (blue) vesicle populations based on size. Both form factors are constant for q > 0.015 Å^{-1}. (H) SANS spectra as a function of % DL at 25°C from 100 nm extruded vesicles. Spectra are offset from the 0% condition for visualization. Solid lines represent best fit of the q > 0.015 Å^{-1} regions using the multilamellar form factor model. The broad shoulder at q ≈ 0.06 - 0.7 is due to the presence of a small population of multi-lamellar vesicles. (I) Bilayer thickness (d_B) as a function of % DL (white circles). Reference SANS data is shown for PC (solid circle, (Kučerka et al., 2011)) and PG (solid square, (Pan et al., 2014)). Calculated d_{PO4s} (solid line) and d_{esters} (dashed line) from coarse-grained molecular dynamics simulations of pure DL/PO 2:1 PE:PG membranes (see **Fig. 3 – Fig. Supp. 1, Source Tables 1-3**).

960

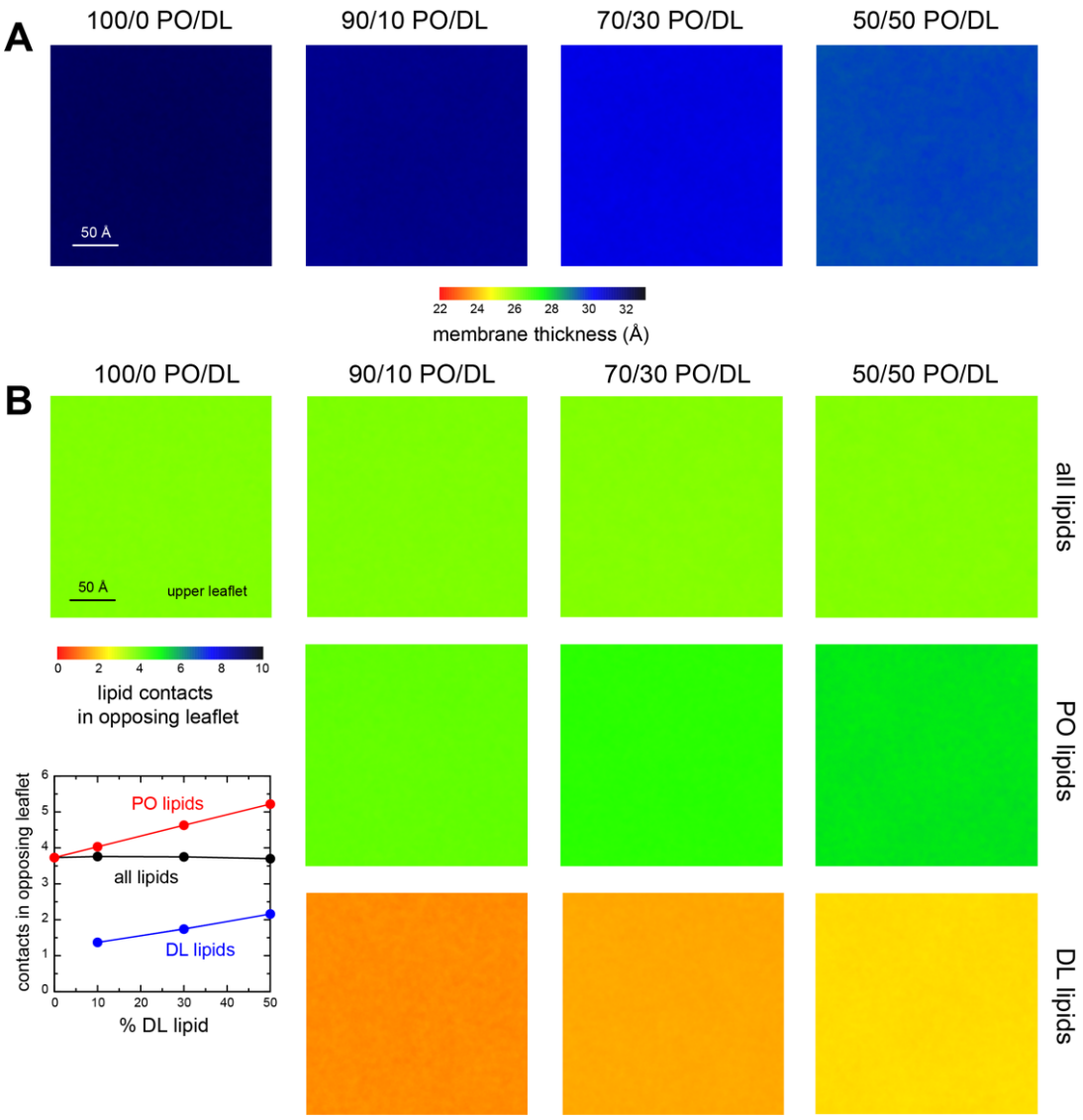

Figure 3 – Figure supplement 1. Evaluation of the thickness of PO:DL bilayers using molecular dynamics simulations. The evaluation is based on CG simulations analogous to those carried out in the presence of CLC-ec1. For each composition, the data shown are averages of 8 independent trajectories of 6-8 μs each (**Fig. 2 – Source Table 1**). All bilayers share a 2:1 PE:PG ratio for the headgroups, but the alkyl-chain lengths differ as the content in short-chain DL lipids increases from 0 to 50%. (A) 2D maps of the local membrane thickness, defined as the difference in the mean Z-coordinate of the ester layers in the outer and inner leaflet. (B) 2D maps of the number of contacts formed by the alkyl-chains in one leaflet with the those in the opposing leaflet, per chain and time-averaged, calculated as in **Fig. 2**. Data is shown combining PO and DL lipids in the analysis, as well as separately for each lipid type. The inset summarizes the 2D data. This data shows that the thickness of the bilayer is ultimately determined by the overall number of interleaflet contacts, which is a constant property for all the mixtures considered. To preserve this constant value upon addition of short-chain DL lipids, the molecular system is driven to increase the number of interleaflet contacts formed by PO lipids, causing the changes in membrane thickness described in panel (A).

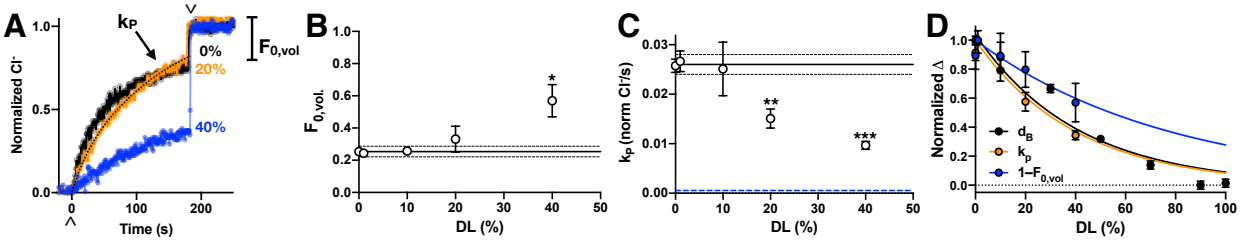

Figure 4. Function of CLC-ec1 in mixed DL/PO lipid bilayers. (A) Traces of chloride transport function in 2:1 PE:PG vesicles containing different proportions of DL vs. PO. Valinomycin initiated chloride efflux (^), and addition of β-OG detergent to dissolve inactive vesicles and release the remaining chloride into solution (v) are marked as shown. Protein was reconstituted at $\chi_{protein}$ = 1 x 10^{-5} subunits/lipid (ρ = 1 µg CLC-ec1 per mg lipids). Numbers show the percentage of DL in the membranes. (B) Fractional volume of inactive vesicles, $F_{0,vol}$. (C) Chloride transport rate, k_P, in normalized Cl^- signal/second. (D) Plot of the normalized change in bilayer thickness, d_B, transport rate, k_P and fraction of active vesicles, $1\text{-}F_{0,vol}$. Fits are single-exponential decays, τ_{db} = 40.94, τ_{kp} = 40.29, $\tau_{1\text{-}F0,vol}$ = 54.07. (See **Fig. 4 - Source Table 1**).

963
964
965
966
967
968
969

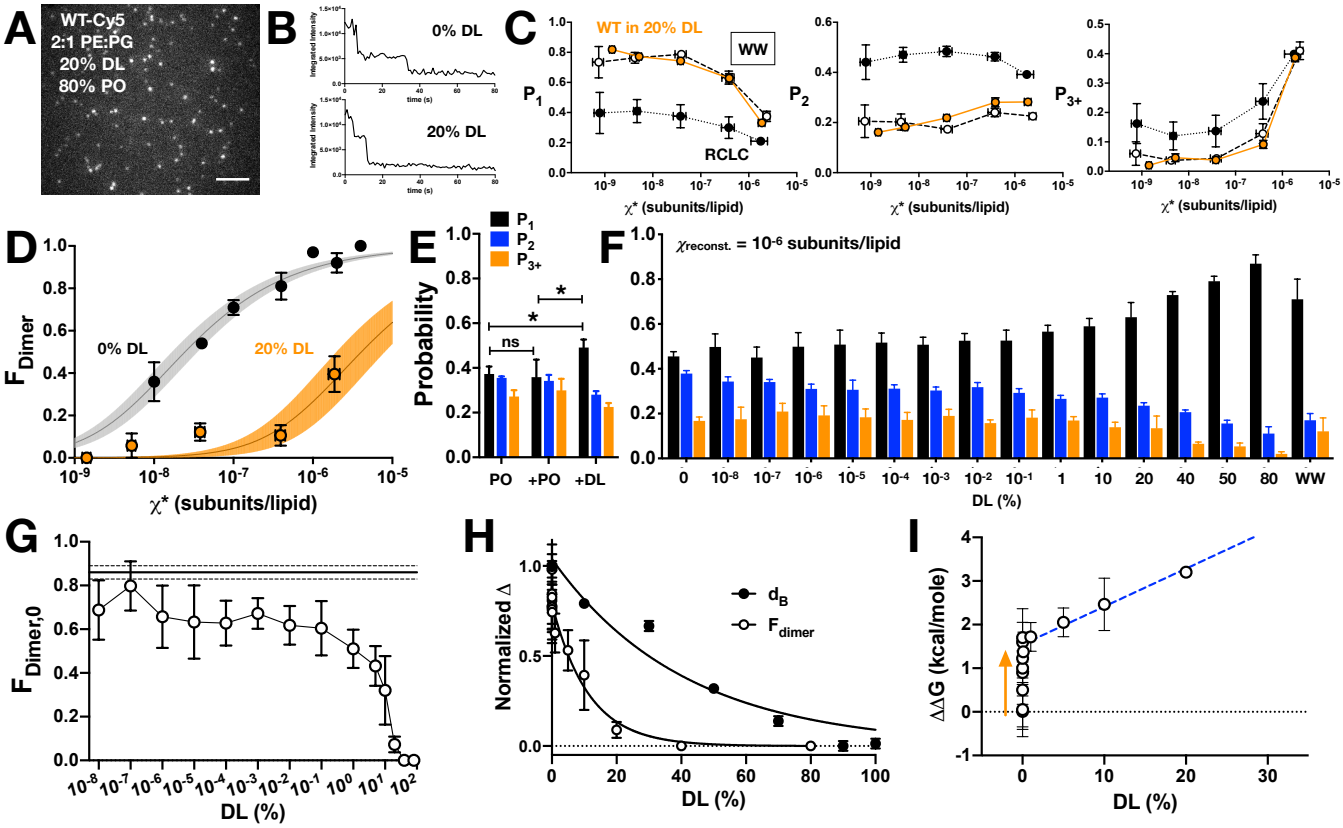

Figure 5. CLC-ec1 dimerization in 2:1 PE:PG membranes with mixed DL/PO acyl chain lengths. (A) Total internal reflection fluorescence microscopy image of 2:1 PE:PG liposomes with 20% DL containing CLC-ec1-Cy5 reconstituted at $\chi_{protein}$ = 1 x 10^{-6} subunits/lipid (ρ = 0.1 μg/mg). Scale bar represents 4 μm. (B) Representative integrated intensity photobleaching traces of WT CLC-ec1-Cy5 in 0% and 20% DL membranes. (C) Photobleaching probabilities *(P_1,P_2,P_{3+})* of monomeric control I201W/I422W-Cy5 (WW, n = 2-3) and dimeric control R230C/L249C-Cy5 (RCLC-Cy5, n = 2-3), and WT CLC-ec1-Cy5 in χ_{DL} = 0.2 (orange circles, n = 2-5) in 20% DL, 400 nm extruded liposomes. Data represented as mean ± sem for the reactive protein/lipid mole fraction χ^* (x-axis) and photobleaching probabilities (y-axis). (D) CLC-ec1 dimerization in 20% DL (orange, $K_{D,20\%DL}$ > 4.1 x 10^{-6} subunits/lipid, $\Delta G°$ = -7.4 kcal/mole, 1 subunit/lipid standard state) compared to previously published 0% DL (black, $K_{D,0\%\ DL}$ = 2.5 x 10^{-8} subunits/lipid, $\Delta G°$ = -10.4 kcal/mole from Chadda et al., JGP 2018), resulting $\Delta\Delta G$ = +3 kcal/mole. (E) Fusion experiment showing the change in the photobleaching distribution of $\chi_{protein}$ = 2 x 10^{-6} subunits/lipid CLC-ec1-Cy5 in 0% DL membranes when diluted 1:1 by fusion with 0% DL or 40% DL, for final 20% DL and $\chi_{protein}$ = 1 x 10^{-6} subunits/lipid conditions. (F) Photobleaching probability distributions of $\chi_{protein}$ = 1 x 10^{-6} subunits CLC-ec1-Cy5 per lipid as a function of % DL ($n_{0\%\ DL}$ = 9; $n_{1E\text{-}8\ to\ 80\%\ DL}$ = 3 - 5; $n_{WW\text{-}Cy5,\ 0\%\ DL}$ = 2 (Chadda et al., 2016). Data represented as mean ± sem. (G) Fraction of dimer, $F_{dimer,0}$, calculated by least-squares fitting of WT-Cy5 distributions to WW-Cy5 and RCLC-Cy5 monomer and dimer controls measured in 0% DL membranes. (H) Normalized change in bilayer thickness (Δd_B) from SANS measurements, compared to fraction of dimers (ΔF_{dimer}) as a function of % DL. Fits are single exponential decays, τ_{db} = 40.94, τ_{Fdimer} = 11.3. (I) $\Delta\Delta G$ vs. % DL, with the two phases indicated by the orange arrow and blue dotted line (slope = 0.087 ± 0.027 kcal/mole per % DL, best-fit ± std. error). See **Fig. 5 - Fig. Supp. 1**, **Source Tables 1-7**.

970

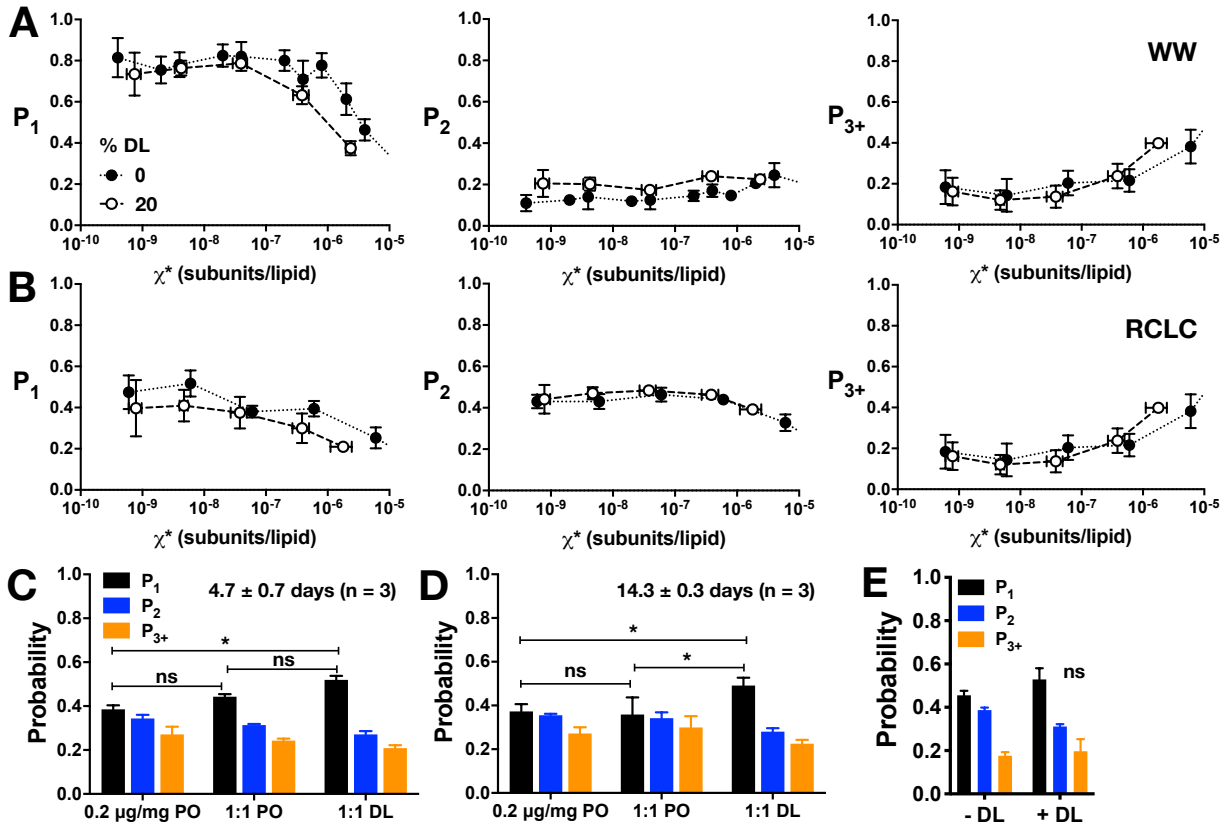

Figure 5 – Figure Supplement 1. Additional analysis of CLC-ec1 assembly in membranes as a function of DL percentage in 2:1 PE:PG membranes. Photobleaching probability distributions *(P_1,P_2,P_{3+})* for (A) WW-Cy5 monomeric control and (B) dimeric control RCLC-Cy5 in 2:1 PE:PG, 400 nm extruded liposomes with 0% DL (black circles) vs. 20% DL (white circles). (C,D) Photobleaching probabilities, P_1 and P_2, for the in-membrane dilution by freeze-thaw fusion of 0.2 µg/mg vesicles in 0% DL membranes (black circles) with either 0% DL (negative control, white circles) or 40% DL membranes for a final DL composition of 20% (orange circles), measured at (C) 4.7 ± 0.7 days and (D) 14.3 ± 0.3 days after freeze/thaw fusion and incubation at room temperature in dark conditions. (E) Comparison of dialyzing 0% DL samples in the absence (- DL) or presence (+ DL) of high DL samples (> 20% DL) in the same dialysis bucket (mean ± sem, n = 3). Distributions are not significantly different.

971
972
973
974
975
976
977
978
979
980
981
982
983

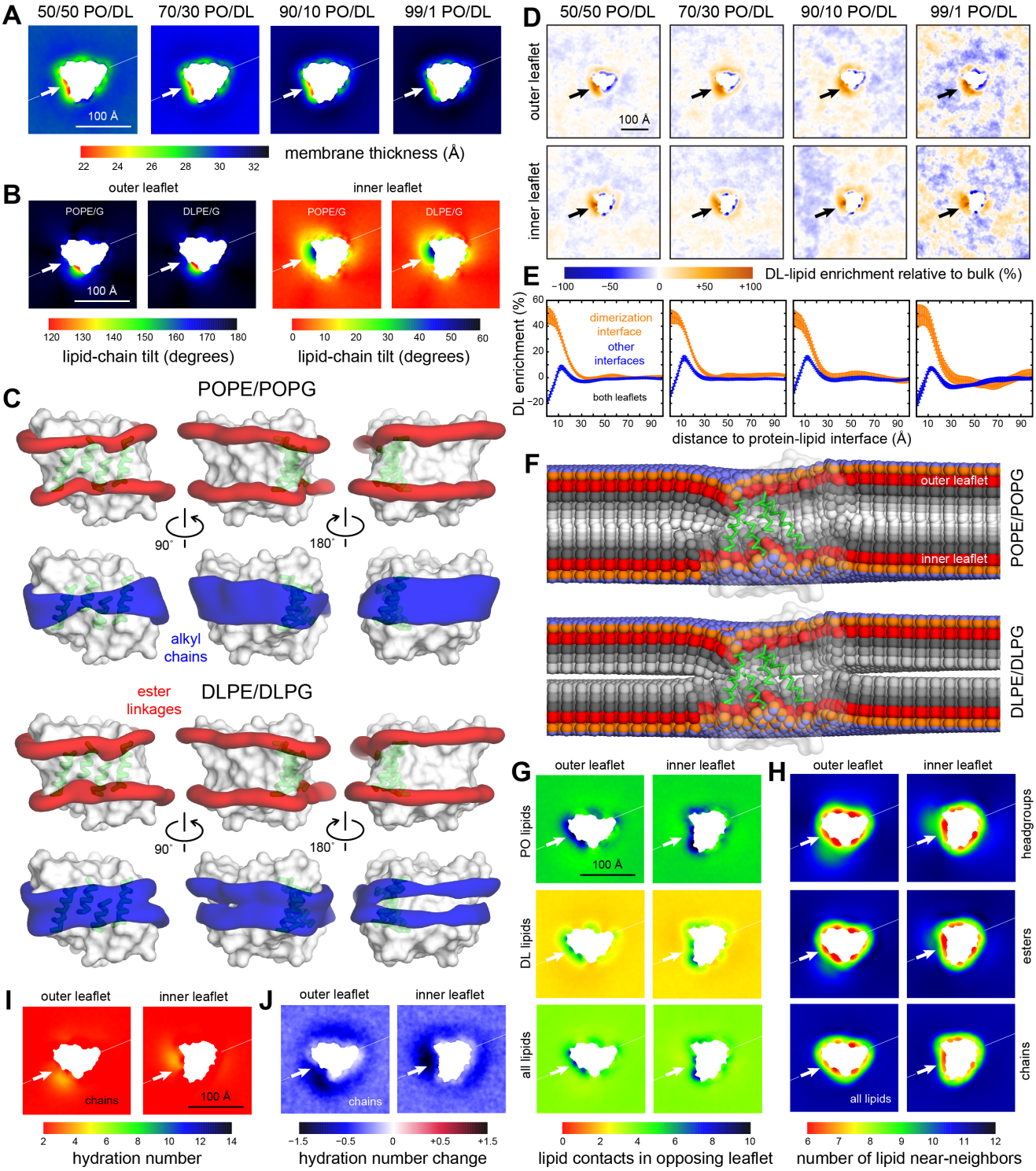

Figure 6. Preferential DL solvation of the CLC-ec1 dimerization interface in mixed DL/PO membranes.
Continued on next page ...

984

Figure 6. Preferential DL solvation of the CLC-ec1 dimerization interface in mixed DL/PO membranes. Data are shown for 2:1 POPE:POPG membranes with varied proportions of 2:1 DLPE:DLPG, namely 1%, 10%, 30% and 50%. For each composition, the results presented are averages of 8 independent trajectories of 6-10 μs each (**Fig. 2 – Source Table 1**) (A, B) 2D maps of the local bilayer thickness and of the mean alkyl-chain tilt-angle, analogous to those shown in **Fig. 2C** for a membrane with no DL. In (B), PO and DL lipids are analyzed separately, and only the 50% DL condition is shown for conciseness. (C) 3D density maps for the ester linkages (red) or alkyl chains (blue) in the vicinity (≤ 10 Å) of the protein (white surface), represented identically to those in **Fig. 2A.** PO and DL lipids are analyzed separately. (D) The percent difference between the observed 2D lipid density ratio (DL/PO) as compared to the expected ratio in the bulk. The data indicate whether DL is accumulated (positive) or depleted (negative) in a specific region of the membrane, relative to what would be expected for the bulk. Each leaflet is examined separately. (E) The results shown in panel (D) are summarized by integrating the data over lipid-solvation shells of increasing width and combining the outer and inner leaflets. Independent profiles are calculated for the dimerization interface and for the other two protein-lipid interfaces. Error bars reflect the standard deviation of the data across independent trajectories. (F) For the 50% DL condition, time-averaged lipid conformations, represented identically to **Fig. 2E**. PO and DL lipids are analyzed separately. (G) For 50% DL, number of contacts formed by the alkyl-chains in one leaflet with those in the opposing leaflet, per chain and time-averaged. PO and DL lipids are analyzed separately or combined as in **Fig. 3 – Supp.1B** and **Fig. 2F**. Note that far from the protein, the total number of interleaflet contacts is identical to that seen for 0% DL, and also identical to that seen for the protein-less membranes irrespective of the DL content. Near the dimerization interface, DL lipids replicate this inherent preference. (H, I) For 50% DL, variation in the number of lipid neighbors in different layers of the membrane, and hydration of the bilayer interior, examined and represented as in Fig. 2G, 2H. Note the drastic reduction in the density defect for the headgroup and ester layers, relative to the 0% DL, and the resulting reduction in water penetration. (J) Quantification of the change in the degree of hydration, as described in Figure 1H, of the alkyl-chains from 0 to 50% DL (note the bulk value is negative because the 50% DL membrane is thinner).

985

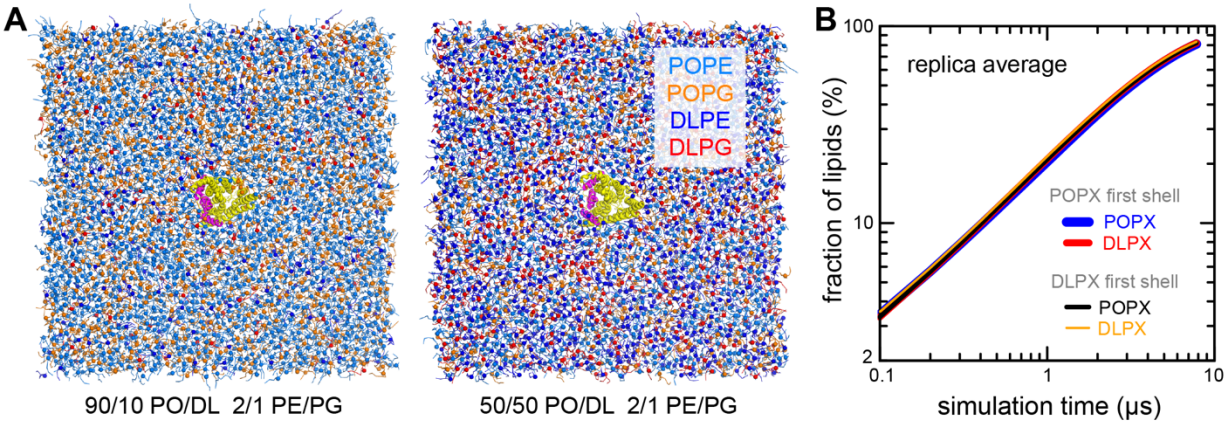

Figure 6 – Figure Supplement 1. Lipid-solvation of the CLC-ec1 monomer in CGMD simulations with PO/DL membranes. (A) Snapshots of simulation systems used to examine the 10% DL (left) and 50% DL conditions. The molecular systems are represented as in **Fig. 2 – Fig. Supp. 1A**. We also examined the 1% and 30% conditions (see **Fig. 2 – Supp. Table 1** for details). (B) Quantification of the degree of lipid mixing observed for the 50% DL condition, evaluated and represented as in **Fig. 2 – Fig. Supp. 1B.**

1032 **SUPPLEMENTARY TABLES**
1033
1034 **Figure 2 – Source Table 1. CGMD simulation specifications.** A total of 0.7 ms total simulation time was carried out for this
1035 study.
1036

	Dimer	Monomer					Pure Membrane			
Component	**100% PO**	**100% PO**	**99% PO 1% DL**	**90% PO 10% DL**	**70% PO 30% DL**	**50% PO 50% DL**	**100% PO**	**90% PO 10% DL**	**70% PO 30% DL**	**50% PO 50% DL**
Protein	2	1	1	1	1	1	0	0	0	0
POPE	1814	1819	1954	1672	1251	839	892	802	616	498
POPG	959	965	977	823	626	425	296	402	320	222
DLPE	0	0	19	214	629	976	0	88	268	448
DLPG	0	0	11	109	343	479	0	46	104	220
Na^+	1898	1710	1377	1696	1730	1514	572	576	554	582
Cl^-	953	748	390	771	764	613	126	128	130	140
H_2O	54,956	35,382	33,150	36,333	37,450	26,814	10,112	10,304	10,444	11,179
System size (nm)	29.4 x 29.4 x 12.0	29.1 x 29.1 x 9.4	30.4 x 30.4 x 8.6	29.0 x 29.0 x 9.5	29.0 x 29.0 x 9.6	27.9 x 27.9 x 8.3	19.9 x 19.9 x 7.4	19.8 x 19.8 x 7.4	19.5 x 19.5 x 7.5	19.5 x 19.5 x 7.6
Number of replicas	10	8	8	8	8	8	8	8	8	8
Simulation time per replica (μs)	9.6 - 12.9	7.4	20.0	6.1	6.0	7.8	6.0	6.7	7.8	6.8
Total simulation time (μs)	107.4	59.1	160.0	55.0	48.3	55.0	48.0	53.6	62.7	54.2

1037
1038
1039
1040 **Figure 3 - Source Table 1. Differential scanning calorimetry for mixed DL/PO 2:1 PE:PG membranes**. Measurement
1041 conducted on liposomes post freeze-thaw in the multi-lamellar state. Data represented as mean ± sem. Statistical differences
1042 compared to the 0% DL samples were analyzed using a student's t-test.
1043

DL (%)	T_m (°C)	n	p-value
0	20.3 ± 0.2	4	
10	18.5 ± 0.4	3	**, 0.0046
30	14.6 ± 0.8	3	***, 0.0005
50	16.1 ± 0.7	3	**, 0.0014
70	19.1 ± 0.4	3	*, 0.0333
100	25.9 ± 0.7	3	***, 0.0004

1044
1045
1046
1047

1048 **Figure 3 - Source Table 2. Cryo-EM radii of 20% DL 2:1 POPE:POPG**. From single preparation of 400 nm extruded vesicles
1049 (n = 1).
1050

r, nm	P_{radius}	F_{SA}	Cumulative F_{SA}
2.5	0	0	0
7.5	0.0129	0.00018	0.00018
12.5	0.0516	0.00201	0.00219
17.5	0.1226	0.00936	0.01155
22.5	0.0387	0.00489	0.01644
27.5	0.0839	0.01582	0.03226
32.5	0.0516	0.01360	0.04586
37.5	0.0839	0.02941	0.07527
42.5	0.07097	0.03197	0.10724
47.5	0.05807	0.03267	0.13991
52.5	0.10323	0.07096	0.21087
57.5	0.03871	0.03192	0.24278
62.5	0.04516	0.04400	0.28678
67.5	0.05807	0.06598	0.35276
72.5	0.03226	0.04229	0.39504
77.5	0.00645	0.00967	0.40470
82.5	0.01290	0.02190	0.42661
87.5	0.00645	0.01232	0.43893
92.5	0.01290	0.02753	0.46646
97.5	0.00645	0.01530	0.48175
102.5	0.01290	0.03381	0.51556
107.5	0.00645	0.01859	0.53416
112.5	0.00645	0.02036	0.55452
117.5	0	0	0.55452
122.5	0.00645	0.02415	0.57866
127.5	0.00645	0.02616	0.60482
132.5	0	0	0.60482
137.5	0.01290	0.06084	0.66566
142.5	0.00645	0.03267	0.69833
147.5	0.01936	0.10502	0.80335
152.5	0.00645	0.03742	0.84076
157.5	0.00645	0.03991	0.88068
162.5	0	0	0.88068
167.5	0	0	0.88068
172.5	0	0	0.88068
177.5	0	0	0.88068
182.5	0	0	0.88068
187.5	0.00645	0.05657	0.93724
192.5	0	0	0.93724
197.5	0.00645	0.06276	1

1051
1052
1053
1054
1055
1056
1057
1058
1059
1060
1061

1062 **Figure 3 - Source Table 3. SANS bilayer thickness analysis for mixed DL/PO 2:1 PE:PG membranes**. 100 nm extruded
1063 vesicles, at 25°C. Data represent best-fit ± standard error. A description of the CGMD analysis is in **Fig. 2 - Supp. Fig. 2.**
1064

	SANS data			CGMD analysis	
2:1 PE:PG	**d_b (nm)**	**d_w (nm)**	**% ULV**	**d_{esters} (nm)**	**d_{PO4} (nm)**
0% DL	3.70 ± 0.02	6.50 ± 0.03	85	3.20	4.06
10% DL	3.55 ± 0.01	5.85 ± 0.03	85	3.15	4.02
30% DL	3.46 ± 0.02	6.11 ± 0.02	85	3.06	3.92
50% DL	3.21 ± 0.01	6.49 ± 0.03	87	2.95	3.81
70% DL	3.08 ± 0.02	6.64 ± 0.03	90	2.85	3.72
90% DL	2.98 ± 0.02	6.65 ± 0.04	90	2.39	3.66
100% DL	2.99 ± 0.02	6.73 ± 0.03	95		
PC	**(Kučerka et al., 2011)**				
0% DL	3.98 ± 0.08				
100% DL	3.30 ± 0.07				
PG**	**(Pan et al., 2014)**				
0% DL	3.85				
100% DL	3.14				

1065
1066
1067 **Figure 4 - Source Table 1. Chloride transport in CLC-ec1 DL/PO proteoliposomes**. Data represent mean ± sem. The
1068 sample n reflects independent protein purifications and reconstitutions, with each single sample averaged over 3 replicated flux
1069 measurements. Statistical p-values are reported for unpaired parametric student t-tests compared to 0% DL data.
1070

DL (%)	$F_{0,vol.}$	p-value	k_P (norm. Cl^-/s)	p-value	n
0	0.25 ± 0.02		0.026 ± 0.001		3
1	0.24 ± 0.01	ns	0.025 ± 0.000	ns	2
10	0.26 ± 0.02	ns	0.023 ± 0.014	ns	4
20	0.33 ± 0.08	ns	0.013 ± 0.001	**, p = 0.008	5
40	0.57 ± 0.10	*, p = 0.046	0.010 ± 0.001	***, p = 0.0001	4

1071
1072
1073
1074
1075
1076
1077
1078
1079
1080
1081
1082
1083
1084

Figure 5 - Source Table 1. Photobleaching data for monomeric control CLC-ec1 I201W/I422W, WW-Cy5 in 20% DL, 80% PO, 2:1 PE:PG lipids. χ^* is the reactive molar ratio of protein subunits and lipids, based on the observed mole fraction calculated from the protein and lipid quantification assays, and assuming the reaction occurs between oriented species in the membrane, $\chi^* = \chi/2$. Data are represented as mean ± standard error. Sample numbers, n, are listed separately for (mole fraction quantification, photobleaching analysis).

density (µg/mg)	χ^* (subunits/lipid)	P_{Cy5}	days	P_1	P_2	P_{3+}	n
0.0001	(8.24 ± 3.07) x 10^{-10}	0.78 ± 0.03	4.0 ± 0.0	0.74 ± 0.11	0.21 ± 0.07	0.06 ± 0.04	(2,2)
0.001	(3.39 ± 0.57) x 10^{-9}	0.77 ± 0.02	3.7 ± 0.3	0.76 ± 0.04	0.20 ± 0.03	0.04 ± 0.00	(2,3)
0.01	(2.92 ± 0.21) x 10^{-8}	0.77 ± 0.02	3.7 ± 0.3	0.79 ± 0.01	0.17 ± 0.01	0.04 ± 0.01	(2,3)
0.1	(2.77 ± 0.31) x 10^{-7}	0.77 ± 0.02	3.7 ± 0.3	0.63 ± 0.04	0.24 ± 0.02	0.13 ± 0.03	(2,3)
0.5	(2.05 ± 0.42) x 10^{-6}	0.78 ± 0.03	4.0 ± 0.0	0.38 ± 0.04	0.23 ± 0.01	0.41 ± 0.03	(2,2)

Figure 5 - Source Table 2. Photobleaching data for dimeric control CLC-ec1 R230C/L249C, RCLC-Cy5 in 20% DL, 80% PO, 2:1 PE:PG lipids. χ^* is the reactive molar ratio of protein subunits and lipids, based on the observed mole fraction calculated from the protein and lipid quantification assays, and assuming the reaction occurs between oriented species in the membrane, $\chi^* = \chi/2$. Data are represented as mean ± standard error. Sample numbers, n, are listed separately for (mole fraction quantification, photobleaching analysis).

density (µg/mg)	χ^* (subunits/lipid)	P_{Cy5}	days	P_1	P_2	P_{3+}	n
0.0001	9.72 x 10^{-10}	0.73 ± 0.02	3.0 ± 0.0	0.40 ± 0.14	0.44 ± 0.07	0.16 ± 0.07	(1,2)
0.001	(4.06 ± 0.53) x 10^{-9}	0.73 ± 0.01	3.7 ± 0.7	0.41 ± 0.08	0.47 ± 0.03	0.12 ± 0.05	(2,3)
0.01	(2.69 ± 0.28) x 10^{-8}	0.77 ± 0.02	3.7 ± 0.3	0.38 ± 0.08	0.48 ± 0.02	0.14 ± 0.05	(2,3)
0.1	(2.77 ± 0.76) x 10^{-7}	0.77 ± 0.02	3.7 ± 0.3	0.30 ± 0.07	0.46 ± 0.02	0.24 ± 0.06	(2,3)
0.5	(1.17 ± 0.48) x 10^{-6}	0.73 ± 0.02	3.0 ± 0.0	0.21 ± 0.00	0.39 ± 0.01	0.40 ± 0.01	(2,2)

Figure 5 - Source Table 3. Photobleaching data for monomeric control CLC-ec1 WT-Cy5 in 20% DL, 80% PO, 2:1 PE:PG lipids. χ^* is the reactive molar ratio of protein subunits and lipids, based on the observed mole fraction calculated from the protein and lipid quantification assays, and assuming the reaction occurs between oriented species in the membrane, $\chi^* = \chi/2$. F_{dimer} is calculated based on the WW-Cy5 and RCLC-Cy5 in 20% DL. Data are represented as mean ± standard error. Sample numbers, n, are listed separately for (mole fraction quantification, photobleaching analysis).

density (µg/mg)	χ^* (subunits/lipid)	P_{Cy5}	days	P_1	P_2	P_{3+}	F_{dimer}	n
0.0001	(1.42 ± 0.17) x 10^{-9}	0.69 ± 0.00	3.0 ± 0.0	0.83 ± 0.01	0.15 ± 0.01	0.02 ± 0.01	0.00 ± 0.00	(2,2)
0.001	(5.23 ± 0.61) x 10^{-9}	0.68 ± 0.01	4.5 ± 1.0	0.77 ± 0.00	0.18 ± 0.02	0.05 ± 0.02	0.07 ± 0.06	(2,4)
0.01	(3.11 ± 0.77) x 10^{-8}	0.68 ± 0.01	4.5 ± 1.0	0.74 ± 0.02	0.22 ± 0.02	0.04 ± 0.01	0.13 ± 0.05	(3,4)
0.1	(4.21 ± 0.44) x 10^{-7}	0.68 ± 0.01	4.5 ± 1.0	0.63 ± 0.03	0.28 ± 0.02	0.09 ± 0.02	0.11 ± 0.05	(3,4)
0.5	(1.87 ± 0.30) x 10^{-6}	0.69 ± 0.00	3.0 ± 0.0	0.33 ± 0.02	0.28 ± 0.01	0.39 ± 0.02	0.40 ± 0.08	(2,2)

Figure 5 - Source Table 4. Shift in dimer equilibrium upon fusion with DL containing vesicles. CLC-ec1-Cy5 proteoliposomes (0.2 µg/mg) in 100% PO, 2:1 PE:PG were either (A) unmodified, (B) fused with 100% PO 2:1 PE:PG liposomes or (C) fused with 40% DL, 60% PO 2:1 PE:PG liposomes by multiple freeze-thaw cycles. Data represented as mean ± sem, n = 3 independent samples. P-values are calculated using the χ^2 test on the (P_1,P_2,P_{3+}) photobleaching probability distributions.

Sample	P_{Cy5}	days	P_1	P_2	P_{3+}	p-value
A: 0% DL, 0.2 µg/mg	0.69 ± 0.01	4.7 ± 0.7	0.39 ± 0.02	0.34 ± 0.02	0.27 ± 0.04	
		14.3 ± 0.3	0.37 ± 0.03	0.35 ± 0.01	0.27 ± 0.03	
B: 1:1 dilution of A with 0% DL		4.7 ± 0.7	0.44 ± 0.01	0.31 ± 0.00	0.24 ± 0.01	ns, p_{AB} = 0.59
		14.3 ± 0.3	0.36 ± 0.08	0.34 ± 0.03	0.30 ± 0.05	ns, p_{AB} = 0.80
C: 1:1 dilution of A with 40% DL		4.7 ± 0.7	0.52 ± 0.02	0.27 ± 0.01	0.21 ± 0.01	*, p_{AC} = 0.03 ns, p_{BC} = 0.28
		14.3 ± 0.3	0.49 ± 0.04	0.28 ± 0.02	0.23 ± 0.02	*, p_{AC} = 0.05 *, p_{BC} = 0.03

Figure 5 - Source Table 5. Photobleaching titration of CLC-ec1 WT-Cy5 in 2:1 PE:PG mixed DL/PO membranes. χ^2 test for (P_1,P_2,P_{3+}) distribution. Data is represented as mean ± sem. $\Delta G°$ was determined from each F_{Dimer} value where $0 < F_{Dimer} < 1$, with $\Delta\Delta G = \Delta G°(x\%\ DL)-mean(\Delta G°(0\%\ DL))$, n in brackets.

% DL (w/w)	P_{Cy5}	days	P_1	P_2	P_{3+}	n	p-value	F_{dimer}	ΔΔG (kcal/mole)
0	0.65 ± 0.01	5.1 ± 0.9	0.46 ± 0.02	0.38 ± 0.01	0.17 ± 0.02	9		0.81 ± 0.05	
1e-8	0.65 ± 0.02	4.0 ± 0.6	0.50 ± 0.06	0.33 ± 0.01	0.18 ± 0.05	4	ns, 0.67	0.69 ± 0.14	0.5 ± 0.9 (4)
1e-7	0.64 ± 0.01	4.3 ± 0.5	0.45 ± 0.05	0.34 ± 0.01	0.21 ± 0.04	4	ns, 0.54	0.80 ± 0.11	0.0 ± 0.6 (4)
1e-6	0.65 ± 0.02	4.0 ± 0.6	0.50 ± 0.06	0.31 ± 0.02	0.19 ± 0.04	4	ns, 0.32	0.66 ± 0.14	1.6 ± 0.4 (3)
1e-5	0.64 ± 0.01	4.3 ± 0.5	0.51 ± 0.06	0.31 ± 0.04	0.18 ± 0.04	4	ns, 0.31	0.63 ± 0.17	1.7 ± 0.5 (3)
1e-4	0.65 ± 0.01	3.6 ± 0.6	0.52 ± 0.04	0.31 ± 0.02	0.17 ± 0.03	5	ns, 0.28	0.63 ± 0.10	0.9 ± 0.7 (5)
1e-3	0.64 ± 0.01	3.8 ± 0.8	0.51 ± 0.03	0.30 ± 0.02	0.19 ± 0.03	4	ns, 0.22	0.67 ± 0.07	1.0 ± 0.4 (4)
1e-2	0.66 ± 0.01	3.3 ± 0.6	0.52 ± 0.03	0.32 ± 0.02	0.16 ± 0.01	4	ns, 0.35	0.62 ± 0.09	1.2 ± 0.5 (4)
0.1	0.65 ± 0.00	3.8 ± 0.8	0.52 ± 0.05	0.29 ± 0.02	0.18 ± 0.04	4	ns, 0.13	0.60 ± 0.11	1.4 ± 0.4 (4)
1	0.65 ± 0.01	3.6 ± 0.6	0.57 ± 0.03	0.27 ± 0.02	0.17 ± 0.02	5	*, 0.036	0.51 ± 0.09	1.7 ± 0.3 (5)
5	0.65 ± 0.01	7.5 ± 3.9	0.59 ± 0.03	0.27 ± 0.02	0.14 ± 0.02	4	*, 0.015	0.43 ± 0.09	2.0 ± 0.3 (4)
10	0.65 ± 0.01	6.0 ± 2.6	0.63 ± 0.07	0.24 ± 0.02	0.13 ± 0.05	3	***, 0.0007	0.32 ± 0.16	2.5 ± 0.6 (3)
20	0.65 ± 0.01	5.0 ± 1.2	0.73 ± 0.02	0.20 ± 0.01	0.07 ± 0.01	4	****, <0.0001	0.07 ± 0.04	3.2 ± 0.0 (2)
40	0.65 ± 0.01	4.5 ± 1.3	0.79 ± 0.02	0.16 ± 0.01	0.05 ± 0.01	4	****, <0.0001	0.00 ± 0.00	ND
80	0.65 ± 0.01	4.5 ± 1.3	0.88 ± 0.03	0.10 ± 0.02	0.02 ± 0.01	3	****, <0.0001	0.00 ± 0.00	ND

Figure 5 - Source Table 6. Testing for DL contamination during dialysis. CLC-ec1-Cy5 proteoliposomes (0.1 µg/mg) in 100% PO, 2:1 PE:PG were dialyzed alone (-DL) or in the presence of a cassette containing > 20% DL (+DL). P-value is calculated using the χ^2 test on the (P_1,P_2,P_{3+}) photobleaching probability distributions. Data is represented as mean ± standard deviation.

sample	P_{Cy5}	days	P_1	P_2	P_{3+}	n	p-value
-DL	0.65 ± 0.02	5 ± 3	0.46 ± 0.06	0.38 ± 0.04	0.17 ± 0.05	9	
+DL			0.53 ± 0.09	0.31 ± 0.02	0.20 ± 0.10	3	ns, 0.22

Figure 5 - Source Table 7. DL and PO concentrations, mole fraction and molality in the titrated DL/PO 2:1 POPE:POPG lipid bilayers. Lipids are prepared at 20 mg/mL total lipid mass, and the % DL mixtures are prepared by combining stock solutions, w/w of total lipid. Note, the headgroup mole fraction remains nearly constant and ranges from χ_{PE} = 0.68-0.69 and χ_{PG} = 0.31-0.32 across the range of % DL studied. MW_{POPE} = 717.996 g/mole, MW_{POPG} = 770.989 g/mole, MW_{DLPE} = 579.746 g/mole, MW_{DLPG} = 632.739 g/mole.

mass ratio	Concentration			Lipid mole fraction		Molality		Protein mole fraction
% DL (w/w)	[Lipid] (mM)	[DL] (mM)	[PO] (mM)	χ_{DL}	χ_{PO}	m_{DL} (moles/ Kg)	m_{PO} (moles/ Kg)	$\chi_{reconst.}$ (subunits/lipid)
0	27.2	0.0	27.2	0.00	1.00	0.00	1.36	1.0e-6
1e-8	27.2	3.4e-9	27.2	1.2e-10	1.00	1.7e-10	1.36	1.0e-6
1e-7	27.2	3.4e-8	27.2	1.2e-09	1.00	1.7e-9	1.36	1.0e-6
1e-6	27.2	3.4e-7	27.2	1.2e-08	1.00	1.7e-8	1.36	1.0e-6
1e-5	27.2	3.4e-6	27.2	1.2e-07	1.00	1.7e-7	1.36	1.0e-6
1e-4	27.2	3.4e-5	27.2	1.2e-06	1.00	1.7e-6	1.36	1.0e-6
1e-3	27.2	3.4e-4	27.2	1.2e-05	1.00	1.7e-5	1.36	1.0e-6
1e-2	27.2	3.4e-3	27.2	1.2e-04	1.00	1.7e-4	1.36	1.0e-6
0.1	27.2	3.4e-2	27.2	0.01	0.99	1.7e-3	1.36	1.0e-6
1	27.3	3.4e-1	26.9	0.01	0.99	1.7e-2	1.35	1.0e-7
5	27.5	1.7	25.9	0.06	0.94	8.4e-2	1.29	9.9e-7
10	27.8	3.4	24.5	0.12	0.88	0.17	1.22	9.8e-7
15	28.2	5.0	23.1	0.18	0.82	0.25	1.16	9.7e-7
20	28.5	6.7	21.8	0.24	0.77	0.34	1.09	9.6e-7
30	29.1	10.1	19.1	0.35	0.65	0.50	0.95	9.4e-7
40	29.7	13.4	16.3	0.45	0.55	0.67	0.82	9.2e-7
50	30.4	16.8	13.6	0.55	0.45	0.84	0.68	9.0e-7
70	31.6	23.5	8.2	0.74	0.26	1.17	0.41	8.6e-7
80	32.3	26.8	5.4	0.83	0.17	1.34	0.27	8.4e-7
100	33.5	33.5	0.0	1.00	0.00	1.68	0.00	8.1e-7